Wesleyan University ⋆ The Honors College

A COMPARISON OF QUANTUM, CLASSICAL, AND EMPIRICAL RATE CONSTANTS FOR VIBROTATIONALLY INELASTIC ATOM-DIATOM COLLISIONS

by

Troy N. Stephens

Class of 1997

A thesis submitted to the
faculty of Wesleyan University
in partial fulfillment of the requirements for the
Degree of Bachelor of Arts
with Departmental Honors in Physics

Middletown, Connecticut ⋆ April, 1997

Abstract

This thesis presents rate constants for nonreactive vibrotationally inelastic collisions in the system Li_2 $A^1\Sigma_u^+ - Ne$, obtained via quantum mechanical computation, classical trajectory simulations, and laser-induced fluorescence experiments. A three-way comparison is made among the results, and comment is made on the relative quality of the quantum and classical modeling. Introductory chapters summarize each of the three methods by which rate constants were obtained.

Acknowledgments

This thesis could not have been without the contributions of many.

Millard H. Alexander, primary author of the *Hibridon* quantum scattering program, assisted me with the use of *Hibridon* and donated his time and his computer time to perform a number of the quantum calculations cited in this thesis.

I am grateful to Professor William Stwalley for the use of the University of Connecticut Laser Facility, whose stable Ti:sapphire lasers enabled us to obtain the experimental data necessary to facilitate this project. Many thanks to Dr. He Wang of the same facility for generous assistance with the lasers that kept our experiments running.

I owe a profound debt of gratitude to Kristin Burgess, Kristin Miller, and Kolo Wamba, for their hard work, sacrifice, and jolly good companionship through the many, many hours of round-the-clock data taking that have provided the experimental basis for this thesis. I wish them all the best in their various future endeavors.

Yunxiao Gao showed me the ropes when I first started out in Brian Stewart's lab, and was great fun to learn from and with.

Kristen Evangelista and Kristin Burgess generously gave their time to read my thesis drafts, and contributed many helpful suggestions during the editing phase of things. Any remaining shortcomings in this document certainly aren't either of their faults.

I thank my parents for support of many kinds, for their faith in me as I have continued to pursue my own, sometimes obtuse path through the yellow

wood, and, most of all now, for their commitment to facilitating my education, no matter the personal sacrifice. Thank you both.

I am grateful to my thesis advisor, Professor Brian A. Stewart, for offering me the opportunity to begin participating in research the summer after my first year at Wesleyan, and the faculty of the Wesleyan physics department for maintaining an environment where this is possible.

In writing this thesis, I have tried to keep in mind R.P. Feynman's advice to thesis writers: "Imagine that you are explaining your ideas to your former smart, but ignorant, self, at the beginning of your studies!" I hope it has benefited in clarity as a result.

Contents

Preface

Almost invariably, on the occasions when I have fielded questions during tours of our lab or talked with people in some other context about the research I've been involved in over the past three years, someone has raised the question: Why is this important? In other words, *what is it good for?* Indeed, this is a reasonable and important question to ask about any research endeavor. I have found that each time I give a slightly different answer, but in all cases the answer could apply equally well to any other area of scientific research. Usually, I try not to feel compelled to justify myself any further than: "Because it is interesting." With a bit more conceit, I can expand on this: "This research is part of humanity's ages-old quest to fully understand Nature." Given the particular field of our research, I find it hard to come up with a directly practical answer ("because what we learn will help us to build a better something-or-other").

Regardless, providing an answer to this question is important not only to justifying the expenditure of resources for the continuation of a research program, but to establishing a context that enables us to understand and appreciate where the work fits into our understanding of the world.

This thesis presents the results of a computational and empirical study of energy transfer behavior in nonreactive inelastic atom-diatom collisions, for a case of low initial vibrotational excitation. Before entering into a description of the technique and analysis of the results, I feel it important to set up the context for this work – so that the reader may at least begin with some sense of its significance within the framework of science, if not *what it is good for*.

Molecular Structure and Collision Dynamics

Collisions involving molecules occur constantly all around us, under everyday conditions. Molecules of nitrogen, oxygen, carbon dioxide, etc. that make up the air that surrounds us are in incessant motion in all directions. The occurrence of collisions between them is an inevitable consequence. At room temperature, a typical air molecule (say, N_2) participates in on the order of 10^{10} collisions per second, traveling only 450 Å or so between collision events.

What makes *molecular* collisions particularly interesting is the fact that molecules possess internal degrees of freedom. These degrees of freedom have internal motions associated with them, and these internal motions have associated energies. When a molecular collision occurs, there is an exchange of energy between the collision partners that may involve a redistribution of the energy associated with the molecule's internal motions.

A *diatomic* molecule is the simplest kind of molecule there is: one composed of only two atoms. In a diatomic molecule, two types of internal motion (besides the motion of electrons) are possible. The constituent atoms may rotate about their common center of mass, and the molecule may vibrate due to the interplay of the internuclear repulsion with the attractive force of the molecular bond. When a diatomic molecule is involved in a collision, its vibrational and rotational energy may be altered. Although they are molecules of the simplest variety, diatoms are sufficiently complex that many aspects of their collisional behavior remain to be fully investigated and still more remain to be well understood.

In a gas at a given temperature, whose constituent particles travel with

a distribution of speeds, collisions occur with a wide range of impact parameters – from head-on impacts (a statistical rarity) to glancing collisions in which one partner scarcely feels the influence of the other. When one or both of the collision partners is a molecule, the relative angular orientation of the collision partners adds another kind of variability. In refining the theory of molecular collision dynamics, we are interested in trying to discern general rules that broadly characterize collision outcomes based on the parameters of a collision, and in understanding – based on the known laws of physics – why the rules we uncover hold true. In particular, we would of course like to find rules that satisfy some intuition we might have about how things ought to work. However, we must be prepared for the fact that Nature may not behave in a way that appeals to our limited sense of what is intuitive. Most of our physical intuition applies to things on a scale where the laws of classical dynamics apply. We begin to develop this intuition the day we are born (if not sooner). In contrast, molecular collisions take place at a scale where the laws of quantum mechanics begin to take over. Typically we do not begin to develop intuition about quantum mechanics until much later in life.

The distinction is important here precisely because the phenomena we are investigating in this project take place in the hazy middle ground that lies between the purely classical and purely quantum worlds. The scale is sufficiently small that we must employ quantum mechanics if we are to model empirical data precisely. Yet it is also sufficiently large that there is hope of extracting some degree of useful and valid insight via a classical analysis, given sufficiently favorable conditions.

It is worthwhile to ask to what extent classical mechanics can offer valid

insights into molecules' collisional behavior at large. This thesis attempts to address this question by examining a case where conditions enable us to make a comparison that includes quantum mechanically computed results as well as classically computed results and empirical data. My hope has been that this comparison will provide one useful data point in the ongoing search for the boundaries of classical theory's applicability.

Methods of Investigation

There are three fundamental avenues open to us in the investigation of molecular collision dynamics. Experiment is of course our guide. In addition, we may attempt to model the collision process using classical or quantum physics (or some hybrid of the two). Both quantum and classical modeling have their respective advantages and limitations, the result being that we would like to have some guidelines for when and how to apply each. The need for such guidelines merits a series of three-way comparisons, such as those presented in this thesis.

Classical modeling, in its basic principles, is easier to grasp conceptually, and yields insights that tend to be more satisfying. Colliding particles follow definite trajectories governed by the the most basic law of Newtonian mechanics: $F = ma$. We can talk meaningfully about the atom striking the diatomic molecule end-on, or impacting off-center from the side, and conclude based on an intuition that seems natural that these events are likely to primarily affect the molecule's vibration or rotation, respectively.[1] And for the most part, one can carry out the necessary calculations using machinery learned as an

[1]We must, however, be careful, because our intuition can sometimes be misleading! A recent classical study by Billeb and Stewart [BS95] indicated, for example, that side impacts in fact provide an important mechanism for *vibrational* excitation.

undergraduate.

In contrast, quantum mechanical modeling of atom-diatom collisions is initially nonintuitive in the ordinary sense. There are no particles and trajectories to think about; only wavefunctions and probability amplitudes. Discussions of individual collision events and geometric configurations lose some of their meaning, and we lose with them the advantage of working in a world where we can study specific interactions being played out over time. Further, the theoretical machinery required to produce quantum mechanical predictions is considerably more involved and computationally intensive. The quantum approach calls for numerical integration of a set of coupled differential equations whose solution must often be cleverly approximated for calculations of any real value to be completed in a reasonable amount of time.

The choice would be an easy one, were it not for the fact that certain important aspects of molecular collision dynamics are only correctly modeled by quantum mechanics. In particular, the vibrational and rotational motions of molecules are *quantized*. Classically speaking, this introduces the counterintuitive notion that a molecule can only vibrate or rotate at particular, allowed frequencies. While an affront to classical theory, this fact emerges as a fundamental consequence in quantum physics, and is plainly evident in the fluorescence spectra we obtain in our experiments. Any study of internal energy transfer in molecular collisions must take it into account. While this quantization of vibrational and rotational states can be partially accounted for without bringing the baggage of a fully quantum mechanical analysis on board, there is no real substitute for a purely quantum treatment when it comes to accurately modeling empirical data.

In short, our dilemma can be summarized as: We'd generally prefer a classical theory. But we can't have one, because Nature doesn't work that way. So we are left to ask, under what conditions can we get away with employing a partly classical analysis? This question provides part of the motivation behind the project discussed in this thesis.

Chapter 1

Goals of the Project

This thesis presents a three-way comparison of rate constants for vibrationally and rotationally inelastic scattering in the system $Li_2 - Ne$, for collisions that originate from the initial molecular state $v_i = 0$, $j_i = 4$ in the $A^1\Sigma_u^+$ electronic state. The rate constants were obtained by quantum mechanical computation, classical modeling, and experiments based on high-resolution laser spectroscopy.

The primary focus of my project has been an investigation into fully quantum mechanical modeling of atom-diatom collisions, via the calculation of rate constants for collisional vibrotational transfer. (The coinage "vibrotational" is hereinafter used to abbreviate the phrase "vibrational and rotational".) While our research group has routinely employed quasiclassical trajectory simulations in the past to provide a model for comparison with empirical data, this project marks the first time our research group has conducted the corresponding quantum calculations. This thesis also represents the first published three-way comparison among quantum, classical, and empirical rate constants for vibrotational transfer in atom-molecule collisions of which we are aware.

A recent paper by Billeb and Stewart [BS95] presented classical computational evidence indicating the presence of two distinct vibrational transfer

mechanisms in $Li_2 - Ne$ collisions, appearing in the form of a bimodal distribution of rate constants for collisions occurring near the velocity threshold where the final vibrational state became accessible (see Fig. 1.1). Experimental data did not provide clear evidence to substantiate this prediction, and it was supposed that the bimodal distribution would only become evident in rate constants for collisions involving low initial vibrotational excitation (v_i and j_i small), due to decreased spectroscopic congestion and the dominance there of the otherwise difficult-to-observe side-impact mechanism for vibrational transfer.

In addition to conducting a general comparison among quantum, classical, and empirical rate constants, this thesis presents the results of an experimental and quantum computational search for verification of the classically predicted bimodal distribution. Thanks to the availability of highly stable tunable lasers operating in the near-infrared, our group was able to obtain rate constant data for $(v_i = 0, j_i = 4)$ and $(v_i = 0, j_i = 18)$ in $Li_2 A^1\Sigma_u^+ - Ne$ last summer. The $(v_i = 0, j_i = 4)$ experiment is well into the regime where the predicted bimodal distribution is expected to be clearly resolvable. It is further to our advantage that the realm of low initial vibrotational excitation is also the one in which the quantum mechanical calculations necessary to obtain rate constants are most computationally feasible. The amount of computer time it takes to solve the coupled-channel equations increases as the cube of the number of open channels. Calculations for very low v_i and j_i are considerably expedited by the fact that few channels are open for downward transfer.

The chapters to follow discuss the various aspects of this project in detail. Chapter 2 discusses the experiment, Chapter 3 the classical modeling, and Chapter 4 the quantum mechanical calculations. While the quantum calculations

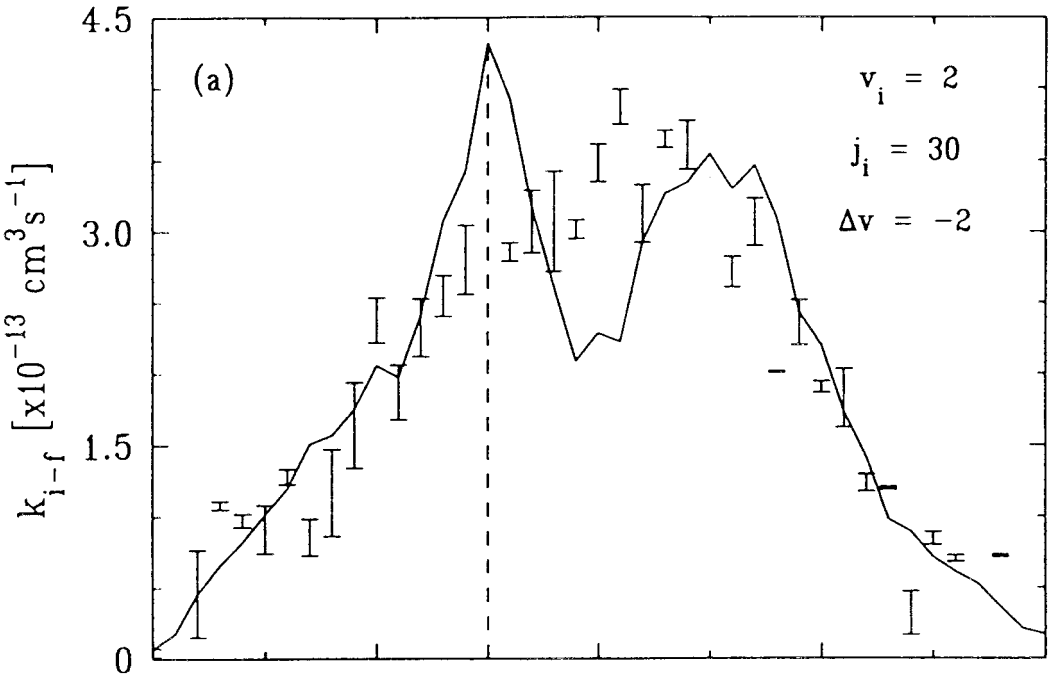

Figure 1.1: Excerpted figure from [BS95], showing experimental (error bars) and scaled quasiclassically computed (solid line) rate constants for $v_i = 2, j_i = 30$ at 691K. Note the clear bimodality of the classically calculated rate constant distribution. The experimental rate constants do not clearly confirm or refute this prediction.

are of particular importance in this comparison, I felt that the foregoing order would most naturally facilitate the introduction and discussion of the concepts relevant to our research. I hope that the reader will agree.

Results are first presented at the end of each of Chapters 2, 3, and 4, then brought together and discussed further in Chapter 5. Three appendices contain the numerical values of the rate constants.

Chapter 2

Experiment

This chapter summarizes our method for experimentally obtaining the rate constants for collisionally induced vibrotational transfer, and presents the rate constants we obtained in our ($v_i = 0, j_i = 4$) Li_2 $A^1\Sigma_u^+ - Ne$ experiment. The details of the experiment implementation and data analysis procedures are already well documented [Go91, Da92, Ga96]. My goal here is to provide sufficient detail to motivate the basic principles that make an experimental determination of the rate constants possible, and to document the features of our ($v_i = 0$,$j_i = 4$) experiment that are unique.

2.1 Essential Principles

The collisions studied in the present experiment are nonreactive vibrotationally inelastic collisions occurring in the $A^1\Sigma_u^+$ electronic state of Li_2, where Ne serves as a structureless atomic collision partner. The qualification "nonreactive" indicates that the reactants equal the products (specifically, the molecule does not dissociate or react), and the term "vibrotationally inelastic" refers to the fact that the Li_2 molecule will absorb or give up vibrational and rotational energy as

a result of a collision.

The process under consideration is summarized by the notation

$$\mathrm{Li}_2 A^1\Sigma_u^+(v_i, j_i) + \mathrm{Ne} \rightarrow \mathrm{Li}_2 A^1\Sigma_u^+(v_f, j_f) + \mathrm{Ne} \tag{2.1}$$

where (v_i, j_i) and (v_f, j_f) signify the initial and final vibrotational states of the molecule, respectively. In practice, we select a particular initial state to probe for the duration of an experiment, and study outcomes of collisions originating from that state. The quantities we seek to obtain in our experiment – the thermally averaged rate constants – essentially provide a probability map that tells us the relative likelihood of a collision leaving a molecule in any particular vibrotational state (v_f, j_f). Since the comparison of these rate constants provides the foundation for the study of molecular collision dynamics documented in this thesis, a precise physical definition of the term *thermally averaged rate constant* and its relationship to known and measurable physical quantities is in order.

2.1.1 Rate Constants

For any given pair of initial (v_i, j_i) and final (v_f, j_f) states, the number of collisionally induced state transitions $(v_i, j_i) \rightarrow (v_f, j_f)$ that occur in a gas per unit density per unit time is a constant quantity. It is therefore meaningful to talk about (and seek to experimentally measure) *rate constants* that express the rates at which various types of collisions occur.

In scattering theory, *cross section* is the fundamental measure of the propensity for a particular outcome to occur. It is expressed in units of area and typically denoted by σ. For vibrotationally inelastic molecular collisions, we can speak of the cross section σ_{if} for collisional transfer of molecules from

an initial vibrotational state (v_i, j_i) to a final state (v_f, j_f). The cross section is a function of the relative velocity $\mathrm{v_{rel}}$ at which a collision occurs: the more energetic the collision, the more energy is potentially available for transfer into higher vibrational and rotational levels, for instance. (Throughout this thesis, I will use $\mathrm{v_{rel}}$ to denote a relative collision speed, to avoid confusion with the vibrational quantum number v.)

A *rate constant* for a bimolecular process, denoted by k_{if} and measured in units of volume per molecule per unit time, is the product of a cross section and the corresponding velocity. A *thermally averaged rate constant* $\bar{k}_{if}$ is a measure of scattering effectiveness [Ba83] that takes into account the thermal distribution of relative speeds at which collisions in a gas occur, by integrating the corresponding cross section over $\mathrm{v_{rel}}$, weighted by this distribution. Specifically,

$$\bar{k}_{if} = \int_0^\infty \mathrm{v_{rel}} \sigma_{if}(\mathrm{v_{rel}})\ f(\mathrm{v_{rel}})\ d\mathrm{v_{rel}} \tag{2.2}$$

where $f(\mathrm{v_{rel}})$ is the collisional speed distribution, as discussed in section 2.1.3. A thermally averaged rate constant also has units of volume per molecule per unit time. While we can't readily isolate collisions occurring at particular speeds in our laboratory in order to measure cross sections, we *can* measure thermally averaged rate constants using the laser-induced fluorescence technique described in section 2.1.2 that forms the basis for the present experiment.

Rate constants are most easily measured under a steady state condition, in which the population density of the level of interest does not change with time. Examination of the steady state rate equation [St87]

$$\dot{n}_f = \bar{k}_{if} n_i n_{\mathrm{X}} + \bar{k}_{if}^{\mathrm{Li}} n_i n_{\mathrm{Li}} - \bar{k}_Q n_f n_{\mathrm{X}} - \Gamma_f n_f = 0 \tag{2.3}$$

that governs population of molecular vibrotational states shows how the ther-

mally averaged rate constants $\bar{k}_{if}$ that we seek relate to known and measurable quantities. Here, n_f specifies the number of molecules per unit volume that are in some particular "final" vibrotational state (v_f, j_f) within the electronically excited state, and $\dot{n}_f$ denotes the time rate of change of n_f. The quantity n_i is the number density of Li_2 molecules in a prepared ("initial") state, n_X is the density of rare gas (Ne) atoms, and n_{Li} is the density of Li atoms.

At the pressures and temperature involved in our experiment (0.85 to 5.9 torr, at 625°C), four competing processes largely control the population and depopulation of a given state, a fact that is reflected in the four terms present in Eq. 2.3.[1] The first term in Eq. 2.3 accounts for population of the final state due to Li_2 collisions with rare gas (Ne) atoms. The second term likewise accounts for the possibility of state-changing collisions with Li atoms in the cell vapor. The third term describes depopulation of the final state due to quenching collisions (collisions that force a return to the ground (X) electronic state). Hence, the constant $\bar{k}_{if}$ is the rate constant for $Li_2 - Ne$ collisions, $\bar{k}_{if}^{Li}$ is the rate constant for Li-Ne collisions, and $\bar{k}_Q$ is the rate constant for quenching collisions. The fourth term in Eq. 2.3 accounts for depletion of the final state due to the process of spontaneous radiative decay that produces the fluorescence we measure in our experiments (as discussed in section 2.1.2). In the fourth term, Γ_f is the reciprocal of the excited state lifetime τ_f. For the A state, $\Gamma_f \approx \frac{1}{18ns}$ [WM77].

[1] This form of the rate equation does not account for the possibility of a molecule undergoing multiple collisions prior to fluorescence back to the ground electronic state, nor does it account for depopulation of the final state due to collisions with Li atoms. These effects are removed in the data analysis procedure, where we employ a more complicated version of Eq. 2.3 that accounts for their contributions. (The conditions of temperature and rare gas pressure in our experiments are also chosen to reduce the probability of a molecule undergoing multiple collisions during the lifetime of its excited state.) Appendix 3.2 of [St87] contains a detailed discussion of these issues.

In a steady state, the population of molecules n_f in any particular final state (v_f, j_f) in A is unchanging, indicated in Eq. 2.3 by the fact that n_f has a zero time derivative.

The rate constants we are interested in obtaining in the experiment discussed in this thesis are the $\bar{k}_{if}$ from the first term that tell us about Li_2 $A^1\Sigma_u^+$ – Ne collision outcomes. These rate constants essentially represent a probability map for going to the various accessible post-collision states. Observing and finding explanations for patterns in these rate constants is key to developing our understanding of nonreactive atom-diatom collision processes.

2.1.2 The Laser-Induced Fluorescence Technique

The collisions we study are of a kind that occur routinely in any gas, due to the random thermal motions of the constituent particles of the gas. Since the collisions require no special stimulus, all that is needed is a means to gather information about their outcomes based on their initial conditions – a means to measure the rate constants. We use a laser-induced fluorescence technique in which the information required to determine collisional rate constants is extracted from spectroscopic measurements. Using a continuous-wave frequency-tunable dye laser, we prepare a population of molecules in a sample cell in a particular initial vibrotational state (v_i,j_i) in an excited electronic state – in this case, the Li_2 $A^1\Sigma_u^+$ state. A molecule excited in this manner will spontaneously decay back to some vibrotational state (v'',j'') in the ground (X) electronic state on the order of 18ns later (the lifetime of the Li_2 A state). In doing so, the molecule emits a photon whose energy equals the difference in energy between the pre-fluorescence and post-fluorescence states. If the molecule is still in the prepared initial state

(v_i,j_i) in A when it decays, the photon energy will simply be the difference in energy between this state and (v'',j'') in the X state.

While in the excited state, however, the molecule has the opportunity to collide with other gas particles as usual. A collision may leave it in some new internal state (v_f,j_f) in the A state.[2] If this is the only collision the molecule undergoes during the lifetime of its electronic excitation, then clearly this will be the state from which it fluoresces. Thus, a notable result of the collision is a change in the set of possible photon energies the molecule can emit when it decays back to the ground electronic state.

From a given state (v',j') in A, the molecule may decay to any of a number of possible states (v'',j'') in X. Conservation of angular momentum requires that $j'' = j' \pm 1$ (i.e. j must change by ± 1 when the photon is emitted, since a photon carries one unit of angular momentum), but there is no similar restriction on v''. Hence the fluorescence resulting from the decay of molecules in some particular final state (v',j') is dispersed to a number of different frequencies.[3]

[2] As noted in the steady state rate equation (Eq. 2.3) it is also possible for a collision to force the molecule back to its ground state. The effects of this type of collision event, called a *quenching* collision, must be accounted for in the course of analyzing the experimental data.

The complementary possibility is for a collision to excite a molecule into a higher electronic state. In the temperature range where our experiments are conducted (610-625°C), the occurrence of a collision of sufficient energy to result in electronic *excitation* of the diatom (or atom) is an exceedingly unlikely event.

[3] I cannot resist briefly explaining something that to me is a beautiful aspect of the experimental work: The tunable lasers we use to populate our initial molecular states operate based on molecular emissions of just the sort we measure in our experiments. The dye molecules in a liquid dye laser are large and complex, with many internal degrees of freedom and extremely dense spectra as a result. They absorb coherent monochromatic light from the "pump" laser beam, and re-emit the energy at a wide variety of frequencies. Fine adjustment of the dye laser cavity length and subsequent filtering optics results in the selection of a single resonant output frequency. The continuous spectrum across the dye's gain curve enables the dye laser to be very finely tuned to any frequency within the dye's range. In effect, we are using the emission spectra of molecules to stimulate *our* molecules into a desired initial state! The Ti:sapphire laser we used in the present experiment works on a similar principle to liquid dye lasers, except that the medium for lasing is a solid crystal. The Ti:sapphire laser yields emission extending

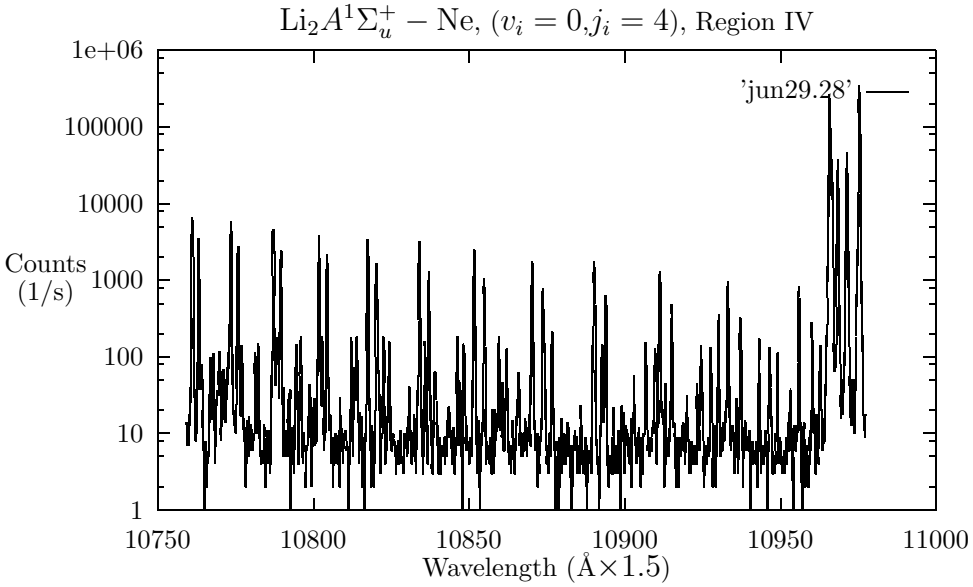

Figure 2.1: A sample scan. Note that the vertical scale is logarithmic.

We obtain our rate constants by looking at comparative strengths of spectral lines seen in the fluorescence spectra. Figs. 2.1 and 2.2 show a sample scan region taken from the data we obtained for ($v_i = 0$,$j_i = 4$). The intensity of each line is proportional to the number of molecules that undergo the corresponding $(v', j') \rightarrow (v'', j'')$ fluorescence transition.[4] The two tallest lines in each figure are called "parent lines", and correspond to fluorescence from the prepared initial state. The conditions of temperature and pressure in this experiment ($T = 625°$C, $P = 0.85$ to 5.9 torr) are such that the most likely event is that no vibration- or rotation-changing collision will occur during the $\sim$ 18ns lifetime of the prepared electronically excited state. Hence these lines have considerably greater intensity than the others, which are termed "satellite

from the red end of the visible spectrum into the near infrared, which is the range of wavelength we need in order to prepare molecules in the A state with small (v_i, j_i).

[4]Strictly speaking, the intensity of a line is given by the area under the line, but the height of the line's peak gives a sufficient measure of the intensity for the purposes of this discussion.

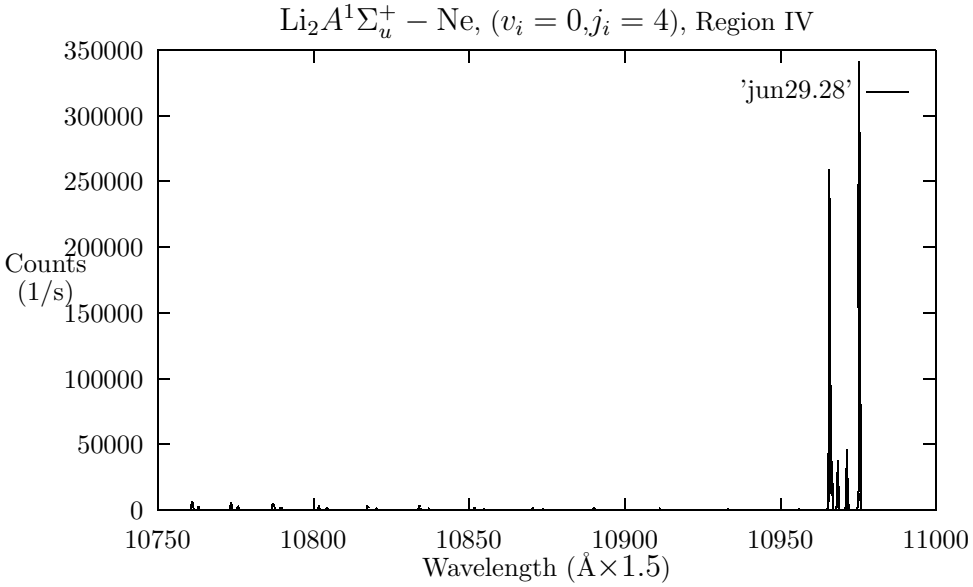

Figure 2.2: The same scan as in Fig. 2.1, plotted with a linear vertical scale to highlight the vastly greater intensity of the 'parent' lines.

lines" and correspond to fluorescence from collisionally populated vibrotational states. By calculating a weighted sum of intensity data[5] for all the satellite lines that originate from a particular (v_f, j_f), and taking the ratio of the result to the net fluorescence intensity out of (v_i, j_i), we can obtain a measure of the population ratio n_f/n_i, which we may note is a ratio of two quantities that appear in Eq. 2.3.

Neglecting for the moment the terms corresponding to Li atom collisions and quenching collisions, Eq. 2.3 can be written as

$$\dot{n}_f = \bar{k}_{if} n_i n_{\mathrm{X}} - \Gamma_f n_f = 0 \tag{2.4}$$

[5]The sum of satellite line intensities for a given (v_f, j_f) is weighted according to each line's transition strength, which expresses the propensity of a Li_2 molecule in the state $(v', j') = (v_f, j_f)$ to undergo the fluorescent transition $(v', j') \rightarrow (v'', j'')$ + photon, as opposed to a fluorescent transition to some other vibrotational state in the ground electronic state. The transition strength is the product of a vibrational band strength, a quantity called the Hönl-London factor (rotational line strength), and the cube of the frequency ν of the photon that is involved, as detailed in [Go91] and [St87].

which, solved for the population ratio n_f/n_i, yields

$$\frac{n_f}{n_i} = \frac{\bar{k}_{if} n_{\mathrm{X}}}{\Gamma_f}. \tag{2.5}$$

The rate constant $\bar{k}_{if}$, then, is the slope of a plot of n_f/n_i vs. n_{X}, multiplied by Γ_f.

In truth, we cannot neglect the effects of Li atom and quenching collisions, so to obtain a particular rate constant we must fit a complete solution for n_f/n_i

$$\frac{n_f}{n_i} = \frac{\bar{k}_{if} n_{\mathrm{X}} + \bar{k}_{if}^{\mathrm{Li}} n_{\mathrm{Li}}}{\bar{k}_Q n_{\mathrm{X}} - \Gamma_f} = \frac{a + b\, n_{\mathrm{X}}}{\Gamma_f + c\, n_{\mathrm{X}}} \tag{2.6}$$

to a set of at least three sample points, and multiply the slope of the fitted curve at zero pressure by Γ_f [Go91, St87]. This requires that we repeat our experiment at a minimum of three pressures. We obtained data at four rare gas pressures in our $(v_i = 0, j_i = 4)$ experiment, providing just enough degrees of freedom for a good fit.

2.1.3 Distribution of Collision Speeds in a Gas

It is important to note that the collisions we observe in our experiment occur with a distribution of speeds that is determined by the temperature of the gas and by the presence of the laser beam used to prepare the initial state. Thermal physics tells us that the particles in a homogeneous gas travel with a distribution of speeds known as a Maxwell distribution

$$f(\mathrm{v}_{\mathrm{rel}}) = 4\pi \left(\frac{m}{2\pi k T}\right)^{\frac{3}{2}} e^{-m\mathrm{v}_{\mathrm{rel}}^2/2kT} \mathrm{v}_{\mathrm{rel}}^2 \tag{2.7}$$

where $f(\mathrm{v}_{\mathrm{rel}})$ is the probability density for a molecule to have speed $\mathrm{v}_{\mathrm{rel}}$, T is the gas temperature in Kelvin, m is the mass of a gas molecule, and k is Boltzmann's

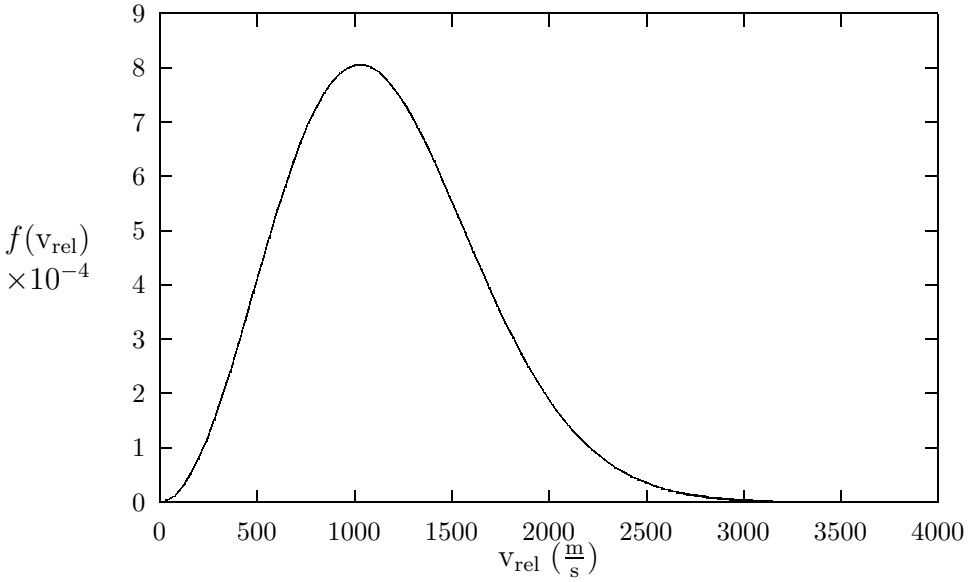

Figure 2.3: Maxwell speed distribution for Li_2 molecules at our experiment temperature of 625°C (898 K).

constant. Fig. 2.3 illustrates such a distribution. A remarkable result is that the distribution of relative speeds between colliding particles in a gas is also a Maxwell distribution. In our rate constant experiments, however, the laser selects only those molecules that have zero velocity component along the beam axis, since any molecule with a nonzero beam axis velocity component will see the beam photons Doppler-shifted, and hence will not (barring the existence of other nearby absorption lines) be electronically excited.[6] Thus we will only see fluorescence for collisions in which the beam-axis molecular velocity component is selected to be zero.[7] As a result, the distribution of observed collision speeds

[6]To be precise, a target state in an atom or molecule has a Lorentzian absorption profile (probability to absorb as a function of photon frequency) that is not infinitely thin, so an incoming photon does not have to be exactly on resonance to be absorbed. However, the absorption profile is sufficiently narrow at our experimental temperature that we select molecules that have essentially no beam-axis velocity component.

[7]This fact is used to our advantage in other experiments we have conducted that measure the velocity dependence (along one axis) of the collisional rate constants by varying the laser frequency [Da92].

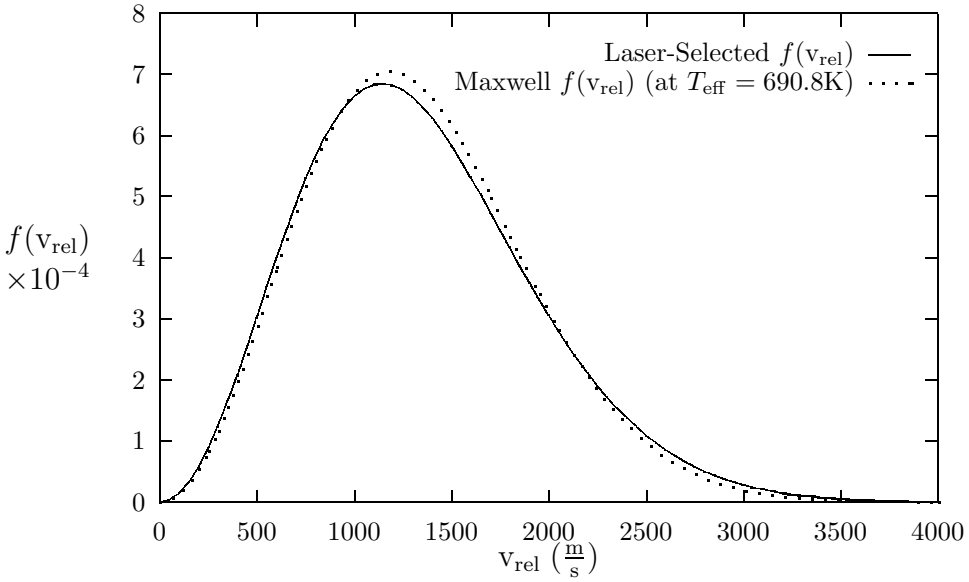

Figure 2.4: Laser-selected speed distribution for $Li_2 - Ne$ collisions (solid line), at our experiment temperature of 625°C (898 K). This distribution is closely fit by a Maxwell distribution with an effective temperature of $T_{\mathrm{eff}} = 690.8$ K (dotted curve).

is not quite Maxwellian, as illustrated in Fig. 2.4. The distribution has the functional form

$$f(\mathrm{v_{rel}}) = \frac{\mathrm{v_{rel}} e^{-\mathrm{v_{rel}^2}/(2r+1)}}{\sqrt{r+1}} \mathrm{erf}\left(\frac{\mathrm{v_{rel}}}{\sqrt{2r(r+1)}}\right) \tag{2.8}$$

in units of $\sqrt{kT/m_{\mathrm{Li_2}}}$, where $r = m_{\mathrm{Li_2}}/m_{\mathrm{Ne}} \approx 0.693$ [GS95, Ga96]. This distribution is closely fit by a Maxwell distribution with an effective temperature of $T_{\mathrm{eff}} = 690.8$ K, as illustrated in Fig. 2.4.

2.2 Details of the Implementation

Issues of practicality dictate a number of the parameters involved in an atom-diatom collisional rate constant experiment, ranging from the selection of collision partners to the setting of conditions of temperature and pressure.

From a theoretical perspective, it is advantageous to study simple diatomics that have few electrons, since many-electron systems are difficult to model accurately. From an experimental standpoint, concerns regarding spectroscopy and strength of the molecular bond come into play. H_2, the simplest of all diatomic molecules, is impractical for us to work with experimentally because of the large energy gap between its ground and first excited electronic states. In a rate constant experiment involving H_2, we would have to excite our initial state using a laser operating in the deep ultraviolet, and detect our molecular fluorescence signal in this same region. He_2 molecules, the next logical choice, only form at extremely low temperatures, because they are incredibly weakly bound. Li_2 is a good candidate for study because its A electronic state is accessible via lasers operating in the visible to near infrared, and it is sufficiently robust that it will not dissociate at the collision energies that occur in our experiments.

The atomic collision partner is selected to be nonreactive and to have a sufficiently large energy gap between its ground and first excited electronic states that it will not be electronically excited at our experimental collision energies. The latter requirement simplifies matters by insuring that the atoms will act as "structureless" collision partners, and will not absorb or give up internal energy as a result of a collision. The noble gases Ne, Ar, Kr, and Xe are common choices.

Lithium is a solid at room temperature, so the sample cell must be heated (to at least 600°C) to provide a sufficient molecular vapor. The rare gas pressure in the cell is also a concern. It must be sufficiently high to produce observable collision activity, yet to better facilitate the data analysis it should be sufficiently low that a prepared molecule does not typically undergo more

than one collision before fluorescing back to the ground electronic state. At our experiment temperature of 625° C and our lowest pressure, 0.85 torr, the time between collisions is of order 80ns, well above the 18ns lifetime of the Li_2 A state. At 5.1 torr, our highest pressure, a molecule typically travels for approximately 18ns between collisions with a rare gas atom, which is equal to the excited state lifetime. Hence, some molecules will certainly undergo multiple collisions prior to fluorescing, especially at the higher rare gas pressures, and we will need to compensate for this effect in the data analysis (as mentioned in footnote 1). In all, however, we can expect fluorescence from molecules that have participated in multiple collisions to account for a reasonably small fraction of the measured fluorescence.

The design of an experiment – the specification of the initial and final states to be studied – is made particularly challenging by a number of essential practical concerns. The initial state excitation must be reachable using an available laser (that is, the frequency of photon required to populate the initial state must lie within the laser's gain curve, or else a multi-photon resonance technique must be employed). The frequency range in which the fluorescence from the post-collision states will be observed must also lie within the range of our detector's sensitivity. When possible, we should also choose a frequency range that is reasonably free from spectroscopic congestion and pollution by spectral lines from sources other than our Li_2 $A \rightarrow X$ fluorescence. Finally, life in the lab is certainly easier if we can operate our lasers in the visible range of the spectrum, since alignment of optics is thereby greatly simplified.

We must also be able to create a significant population in the desired initial state (v_i, j_i) in A. Two factors come into play here. First, collisions

among molecules set up a thermally populated distribution of vibrotational states (v_X, j_X) in the X state. To facilitate getting a large number of molecules into the desired vibrotational state (v_i, j_i) in A, it is desirable to choose a well-populated vibrotational state (v_X, j_X) to excite *from*. The second consideration is the strength of the electronic transition between our chosen vibrotational state (v_X, j_X) and the target state in A we wish to prepare. The value of the overlap integral between the two states' vibrational wavefunctions ψ_X and ψ_A, called the Franck-Condon Factor (FCF), provides a good measure of the electronic transition strength. The larger this quantity, the larger the excited-state population we get. And a larger population means cleaner, more reliable data.

We obtain our fluorescence spectra by scanning a double monochromator across the frequency ranges where the lines of interest reside. A photomultiplier tube (PMT) connected to a photon counter (essentially a current pulse counter) enables us to measure line intensities as the number of photons of each monochromator-selected frequency detected in a specified integration time.[8]

2.3 Particulars of the $(v_i = 0, j_i = 4)$ Experiment

Exciting to the $(v_i = 0, j_i = 4)$ level in the Li_2 A state requires a frequency- and intensity-stable tunable laser operating in the near infrared, at 14010.1866 cm^{-1} (714 nm). Such lasers are hard to come by, and we have been fortunate during the course of the past two summers to have the use of lasers at the University of Connecticut, Storrs, laser facility that meet these criteria. Our initial molecular state was prepared using a Coherent 899 ring laser operating with a Ti-sapphire

[8]Feynman's *QED: The Strange Theory of Light and Matter* contains a beautiful description of how it is that a PMT can detect individual photons.

dye/crystal	frequency range (cm^{-1})
Ti:MW	11000-12600
Ti:SW	12100-14250
LD700	12800-14350
DCM	14300-15850
KR620	15380-16400
R6G	16100-17700
R110	17500-18950
S3	21505-23800

Table 2.1: Operating ranges of various laser dyes and crystals. The laser used in the present experiment was a Ti:SW.

crystal and producing 250 mW stabilized output power, pumped by a Coherent Innova 200 Ar^{++} laser producing 13.1 W output power at 42.2 A input current. Table 2.1 shows ranges for a variety of available laser dyes and crystals. We were operating near one end of the Ti:SW gain curve, but encountered less difficulty in maintaining frequency and power lock than we anticipated in doing so. The laser behaved exceptionally well, operating through most of the 24 hour data-taking procedure with no adjustments needed for hours at a time.[9] Since reasonable constancy of laser frequency and power delivery throughout the course of a roughly 20-minute scan are essential to obtaining meaningful data, and laser mode hops (sudden jumps to another lasing frequency) require that a scan be aborted and redone, this kind of stability was key to making the present experiment a success.

Some degree of drift in laser frequency and power is inevitable, and a

[9]One thing I have learned about tunable lasers the hard way: the less they are disturbed, the more steady their performance. Most of the times we lost frequency lock were due to unnecessary human tampering.

region	frequency range (cm^{-1})
I	11830-11997
II	11996-12159
III	11118-11280
IV	10760-10978
V	10960-11160

Table 2.2: Scan regions for the $(v_i = 0, j_i = 4)$ experiment. The overlap between regions – in some cases slight, in others substantial – is due to the need to include at least one parent line in each scan for the purpose of line intensity normalization.

means is needed to correct for the effect such drifts have on the measured fluorescence line intensities. As has been done in previous experiments, we conducted a short scan over a parent line before and after each region scan. An overall change in parent line intensity of roughly 5% or less over the course of a scan is corrected for during the data analysis procedure, by adjusting line intensities across the scan region via linear interpolation. (This assumes that the drift in signal strength is linear.) A change of more than about 5% in the parent line intensity calls for a scan to be redone.

Fluorescence data were recorded at each of four rare gas pressures (5.09, 3.44, 1.81, and 0.86 torr), in the frequency regions listed in Table 2.2. The entire experiment was conducted at a stabilized gas temperature of 625 ± 1°C (898 K).

2.4 Results

The rate constants I obtained for $\Delta v = 0 - 2$ by analysis of our $(v_i = 0, j_i = 4)$ experiment data are plotted in Figs. 2.5-2.7, as a function of the final rotational

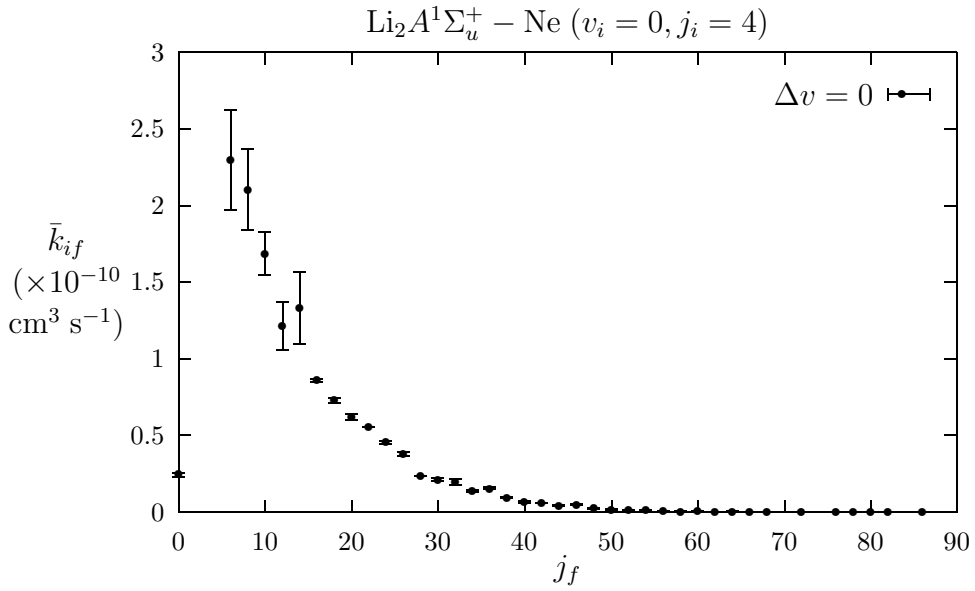

Figure 2.5: Experimentally obtained thermally averaged rate constants $\bar{k}_{if}$ for $\Delta v = 0$

quantum number j_f. The numerical values of the experimental rate constants are given in Appendix B. The order of magnitude of the rate constants is consistent with data we have obtained for other (v_i, j_i) in the past (c.f. [Go91]).

A number of interesting features in the rate constants are readily noted. The rate constants for $\Delta v = 0$ (Fig. 2.5) show the clearest progression, decreasing smoothly as Δj increases from 2 ($j_f \geq 6$), as should be expected since few collisions occur with sufficiently high energy to produce high rotational excitation.[10] A similar trend is visible in the $\Delta v = 1$ rate constants, although in this case the rate constants peak around $j_f = 20$ instead of at $j_f = j_i = 4$. It is evident from this plot that a vibrational transfer of $\Delta v = 1$ is likely to be accompanied by rotational transfer – most probably a Δj of +16 or so.

[10]The error bars for $j_f = 6 - 14$ in the $\Delta v = 0$ rate constants appear conspicuously large, but the errors are in fact not particularly large relative to the sizes of the rate constants (see Appendix B).

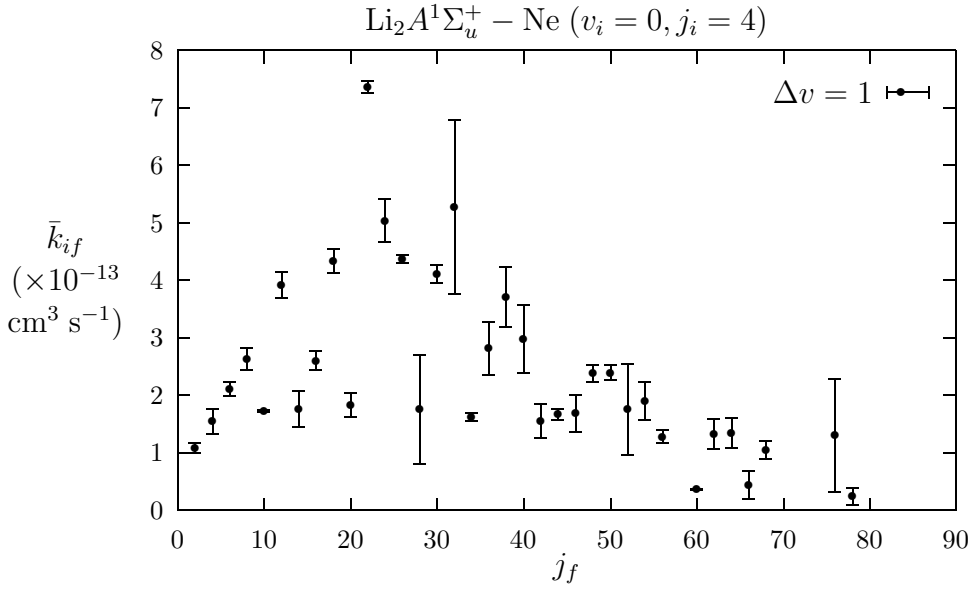

Figure 2.6: Experimentally obtained thermally averaged rate constants $\bar{k}_{if}$ for $\Delta v = 1$

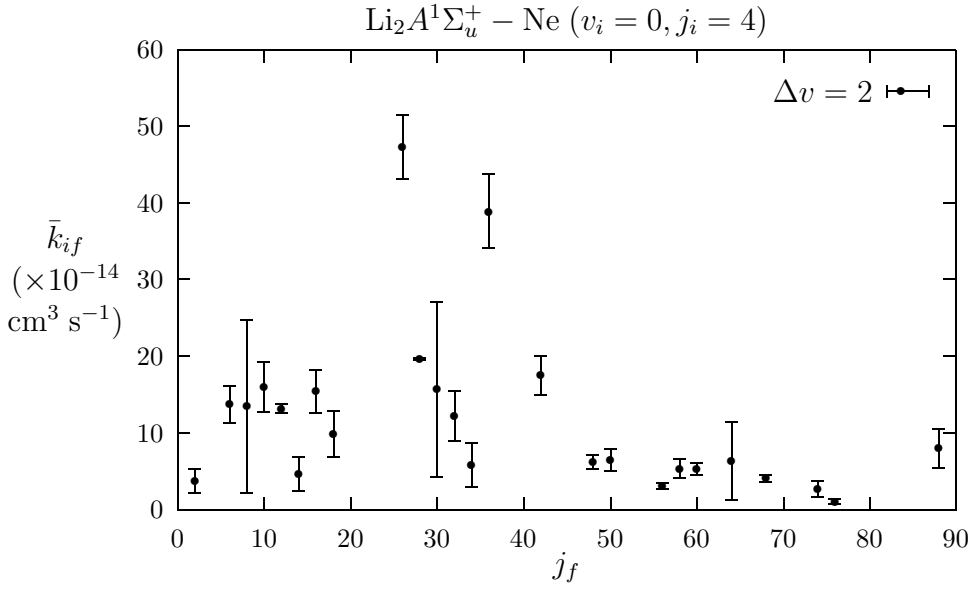

Figure 2.7: Experimentally obtained thermally averaged rate constants $\bar{k}_{if}$ for $\Delta v = 2$

The distribution patterns of the rate constants for $\Delta v = 1$ and $\Delta v = 2$ are not as readily discernible as for $\Delta v = 0$. These rate constants, particularly those for $\Delta v = 2$, are more subject to error than the $\Delta v = 0$ rate constants, due to the smaller intensities of the corresponding spectral lines (the smallest assignable lines being 10^{-4} the parent line intensity, or approximately 30 counts per second). Given that such small lines are especially subject to pollution by PMT background noise and other nearby lines (c.f. Fig. 2.1), the difficulty of correctly identifying the lines and extracting accurate intensities for them is accentuated. For the $\Delta v = 1$ case, there is a curious aggregation of rate constants around 1.8×10^{-13} cm^3 s^{-1}, seemingly superimposed on a primary distribution that peaks around $j_f = 20$. I am presently uncertain whether this is an artifact of erroneous line assignment on my part, a result of the relatively poor data available for $\Delta v \neq 0$, or a feature indicative of some significant collisional phenomenon. Based on data previously obtained and analyzed in our group, and the fact that this experiment marks the first time I have attempted to analyze the data myself, I am more inclined to believe one of the first two explanations. A more meticulous, band-by-band analysis (in which each vibrational fluorescence band $v' \rightarrow v''$ is examined separately) may shed light on the nature of this feature by improving the quality of the extracted rate constants. The expectation is that a more clearly defined pattern to the rate constants for $\Delta v \neq 0$ should emerge. Whether this pattern will display a clear bimodal character is uncertain at this point, but seems unlikely based on preliminary work we have done toward a complete band-by-band re-analysis of the fluorescence spectra.

The experimentally obtained rate constants are discussed further in Chapter 5, in the context of comparison with the rate constants we obtained

by quantum mechanical and classical computational methods.

Chapter 3

Classical Mechanics

In our theoretical calculations – both classical and quantum mechanical – the goal is to obtain predictions of the thermally averaged rate constants $\bar{k}_{if}$. This chapter provides a brief outline of the classical method for obtaining the collisional rate constants, and presents my classically computed results for ($v_i = 0, j_i = 4$) in Li_2 $A^1\Sigma_u^+ - Ne$.

3.1 Classical Trajectory Simulation

Classical physics offers us the opportunity to study the courses and outcomes of individual atom-diatom collisions in detail. Given a function $V(q_1, \ldots, q_N)$ that specifies the potential energy of our interacting atom-diatom system as a function of the system's coordinates $(q_1, \ldots, q_N)$, and a particular choice of initial positions $(q_{i1}, \ldots, q_{iN})$ and momenta $(p_{i1}, \ldots, p_{iN})$, we can compute the classical trajectory that collision partners with the given initial conditions would follow, via numerical solution of a set of differential equations. (Hamilton's equations are one popular choice, but any equivalent formulation of classical dynamics will do.)

Each of the rate constants $\bar{k}_{if}$ that we measure in an experiment, however, constitutes the collective signature of collisions occurring in a large statistical ensemble, with a variety of relative speeds and impact parameters. To generate a set of thermally averaged collisional rate constants suitable for comparison with our experiment results, it is therefore necessary to bridge the gap between the study of individual collision trajectories and the macroscopic view that is concerned with many collisions occurring continually in a steady state. We must also somehow account for classical dynamics' neglect of the important fact that the molecule's vibrational and rotational states are quantized.

Quantization is simulated through a process called "binning", in which the molecules coming out of trajectory runs are sorted into bins according to their final vibrational and rotational actions. A variety of approaches to implementing this process have been used, all of which perform the same basic task. Each trajectory is run until the collision partners move far enough apart that their mutual interaction becomes negligible. The molecule's final vibrational and rotational actions are then determined, and the molecule is assigned to the quantum vibrotational state (v_f, j_f) that provides the closest match to these values.

The task of accounting for the macroscopic character of the experimental data is in part accomplished by running a large number of trajectories (on the order of 10^5 or more) with a suitable pseudo-random distribution of initial position and momentum coordinates that is designed to be representative of molecules in the initial state (v_i, j_i) of interest. Through the binning process, we accumulate statistics regarding the collisional population of final states. However, we must also be sure to account for the thermal (and partly laser-selected) distribution

of speeds at which the collisions occur. This is achieved using a technique called Gauss-Laguerre integration, as described in the following section.

3.2 Gauss-Laguerre Quadrature

Each batch of trajectories is run at a specified collision speed and initial state (v_i, j_i). To take into account the speed distribution of the collisions that contribute to our experimentally measured rate constants $\bar{k}_{if}$, we must in principle integrate cross sections $\sigma_{if}(\mathrm{v_{rel}})$ calculated at all possible relative collision speeds, weighted by the experimental speed distribution $f(\mathrm{v_{rel}})$ (see Eq. 2.8 and Fig. 2.4):

$$\bar{k}_{if} = \int_0^\infty \mathrm{v_{rel}} f(\mathrm{v_{rel}})\ \sigma_{if}(\mathrm{v_{rel}})\ d\mathrm{v_{rel}}. \tag{3.1}$$

Clearly we cannot hope to calculate rate constants at *all* possible collision speeds, and since running 10^5 trajectories (a comfortable minimum statistical base) at a given energy takes approximately 24 hours on the workstation we currently use for our classical calculations, it is desirable to minimize the number of different speeds at which the rate constants must be sampled in the course of getting an accurate value for the integral. This is achieved using the technique of Gaussian quadrature, in which a careful selection of representative collision speeds permits the value of the integral in Eq. 3.1 to be approximated by a finite sum: [ArWe95]

$$\bar{k}_{if} = \int_0^\infty \mathrm{v_{rel}} f(\mathrm{v_{rel}})\ \sigma_{if}(\mathrm{v_{rel}})\ d\mathrm{v_{rel}} \approx \sum_{i=1}^{n} w_i\ \sigma_{if}(\mathrm{v_{rel},}_i) \tag{3.2}$$

where the w_i are constant weighting coefficients that take the place of the weight function $f(\mathrm{v_{rel}})$. In the Gauss-Laguerre version of this technique, the sample points $\mathrm{v_{rel},}_i$ are chosen according to the zeros of the Laguerre polynomials, a criterion which maximizes the accuracy of the finite sum approximation. Table 3.1

i	$v_{\mathrm{rel},i}$ $(\frac{\mathrm{cm}}{\mathrm{s}})$	E (cm^{-1})	w_i
1	36260.5	55.2027	.02036302
2	83322.5	249.1503	.1686041
3	130879.3	600.2090	.3197351
4	178847.5	1112.2166	.2869802
5	227335.4	1790.9502	.14746361
6	276495.6	2644.5274	.04646192
7	326516.9	3684.0297	.00917319
8	377633.1	4924.4478	.0011301704

Table 3.1: Sample speeds determined by the Gauss-Laguerre integration, and their associated weights w_i. The third column gives the kinetic energy corresponding to each collision speed, expressed in wavenumbers (cm^{-1}). These are the first eight points of a sixteen-point Gauss-Laguerre integration.

lists the speeds selected for comparison with our experiment, and the associated weights for the Gauss-Laguerre integration. Fig. 3.1 provides a graphical illustration of the weighting. For my calculations, I truncated the sum after the first eight terms, since subsequent terms contain successively more negligible weights. This approximation method is not without its shortcomings, but provides a generally good compromise between accuracy and computational demand. The single *caveat* is that, while calculations for collisions occurring at higher speeds do not stand to contribute much to the integration based on the smallness of their weights, such calculations are also potentially important because of the opening of new final vibrotational states that comes with the increase in the collision energy. While the relative quickness of the classical rate constant calculations would permit the addition of higher collision speeds without much additional cost, the rapid growth in the time complexity of the quantum mechanical calculations with collision speed (as discussed in Chapter 4) would make the addition of many higher speeds impractical for the case where vibrational inelasticity is

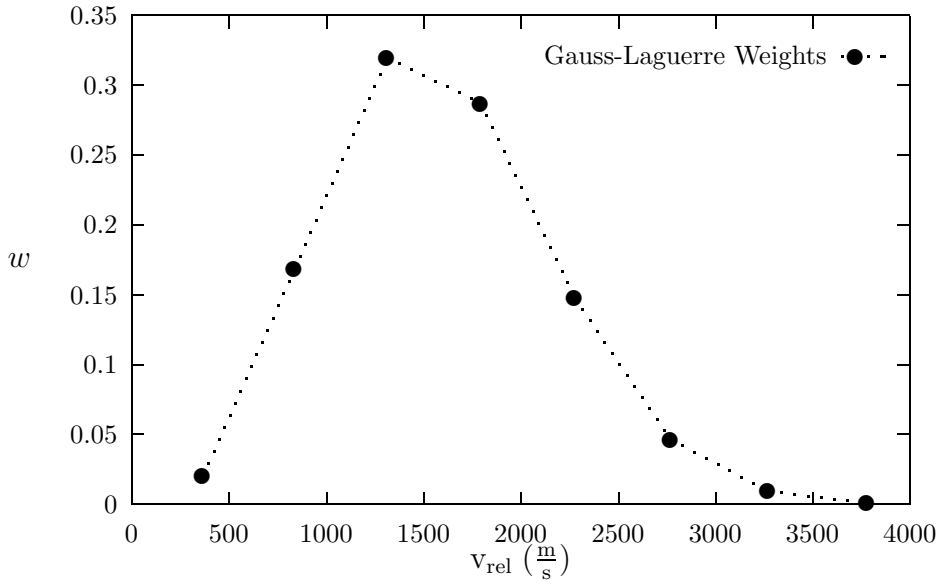

Figure 3.1: Plot of the Gauss-Laguerre weights for the eight sample energies at which classical trajectories were run to compute collisional rate constants.

included. Hence I ran calculations at only the first eight Gauss-Laguerre speeds for the comparison presented in this thesis.

3.3 Execution

I ran 100,000 trajectories for $(v_i = 0, j_i = 4)$ in Li_2 $A^1\Sigma_u^+ - Ne$ at each of the four highest Gauss-Laguerre speeds, and half that many of each of the four lowest speeds. (More energetic collisions open a larger number of final vibrotational states to transfer, and hence require a larger number of trajectories to be run to accumulate a good statistical base.) The trajectories were computed based on the action-angle method of Smith [Sm86], using the standard histogram binning method [Pa79], and a highly accurate *ab initio* Li_2 $A^1\Sigma_u^+ - Ne$ potential energy surface (PES) due to Alexander and Werner [AW91]. The program that ran the calculations was originally developed by Neil Smith and has been routinely used

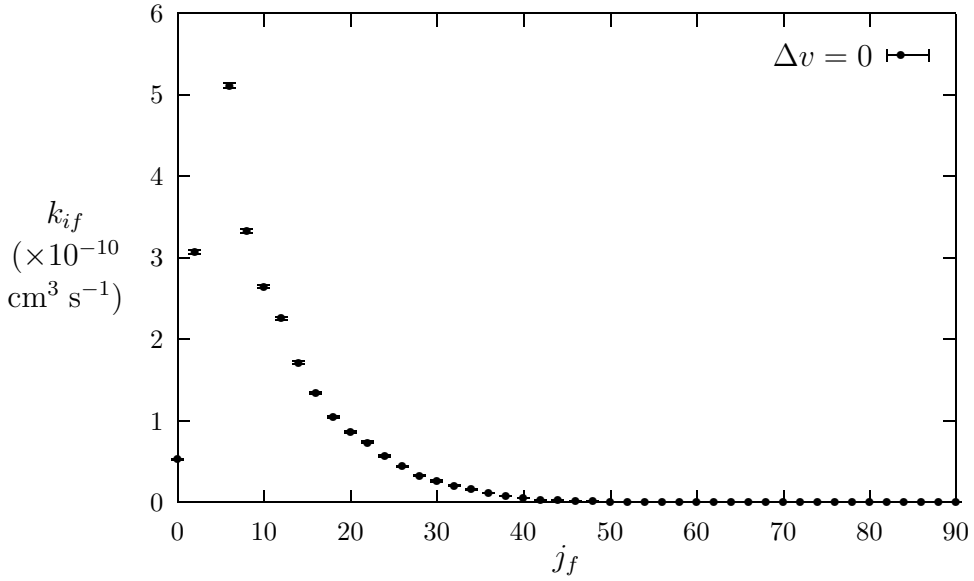

Figure 3.2: Classically computed thermally averaged rate constants for $\Delta v = 0$

and extended by our research group. Cross sections obtained at each of the eight sample speeds were combined via the Gauss-Laguerre weighted sum to obtain the thermally averaged rate constants $\bar{k}_{if}$.

3.4 Results

The rate constants I obtained via classical trajectory calculations are plotted in Figs. 3.2-3.4, with corresponding cross sections shown in Figs. 3.5-3.7. The numerical values of the classically computed rate constants are given in Appendix C.

Fig. 3.6 demands immediate mention. Here, in the cross sections calculated at energies 7 and 8, we see a clear bimodal distribution much like that observed by Billeb and Stewart in classical rate constant calculations for $(v_i = 2, j_i = 30)$ in Li_2 $A^1\Sigma_u^+ - Ne$, at $\Delta v = -2$ [BS95]. Here, the bimodality washes out in the Gauss-Laguerre integration, and hence is not clearly discernible

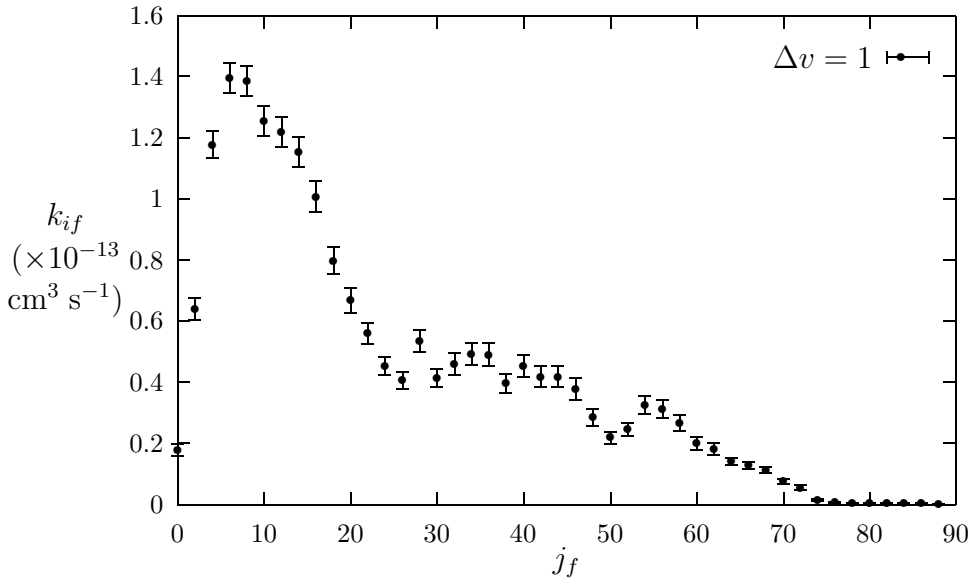

Figure 3.3: Classically computed thermally averaged rate constants for $\Delta v = 1$

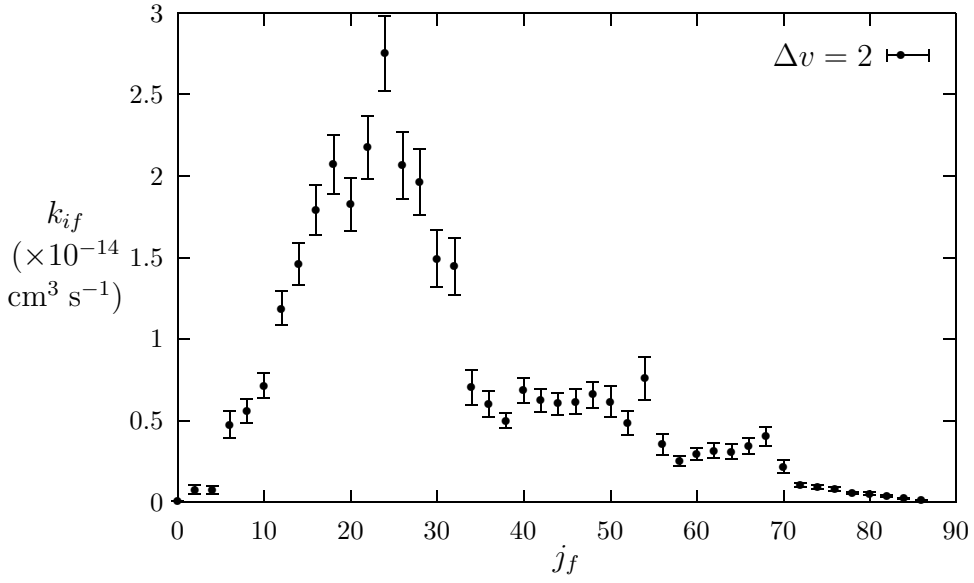

Figure 3.4: Classically computed thermally averaged rate constants for $\Delta v = 2$

in the rate constants for $\Delta v = 1$, but its presence in the cross sections is certain.

The classical rate constant plots contain a number of interesting features. The purely rotationally inelastic ($\Delta v = 0$) rate constants peak on either side of $j_f = j_i = 4$, and fall off smoothly but rapidly with increasing j_f, consistent with the behavior of the experimental $\Delta v = 0$ rate constants. The rate constants for $\Delta v = 1$ and $\Delta v = 2$ appear to peak near $j_f = 6$ and $j_f = 20$, respectively, possibly implying a trend wherein higher vibrational transfer tends to be accompanied by higher rotational transfer. This would make sense from the classical perspective, since the wide energetic spacing of vibrational levels relative to rotational levels means that high kinetic energies are necessary to induce upward vibrational transfer, in which case the correspondingly high momentum transfer, even when multiplied by a small moment arm, would be sufficient to induce upward rotational transfer as well.

Small-scale fluctuations visible in the rate constants as a function of j_f, most visible in the $\Delta v = 1$ and $\Delta v = 2$ rate constant plots, are due largely to the bimodal character of the cross sections for $\Delta v = 1$, coupled with the fact that the weighted integration over collision speed was approximated by a finite Gauss-Laguerre sum with a small number of terms. This can be seen from examination of Figs. 3.6 and 3.7), which show the classically computed cross sections from which the $\Delta v = 1$ and 2 rate constants were calculated. The cross sections peak in different locations at each energy, which gives rise to small "humps" when the cross sections are combined via the Gauss-Laguerre sum to yield the thermally averaged rate constants.

Further scrutiny of the classically computed rate constants is deferred until Chapter 5, where the three-way comparison among empirically obtained,

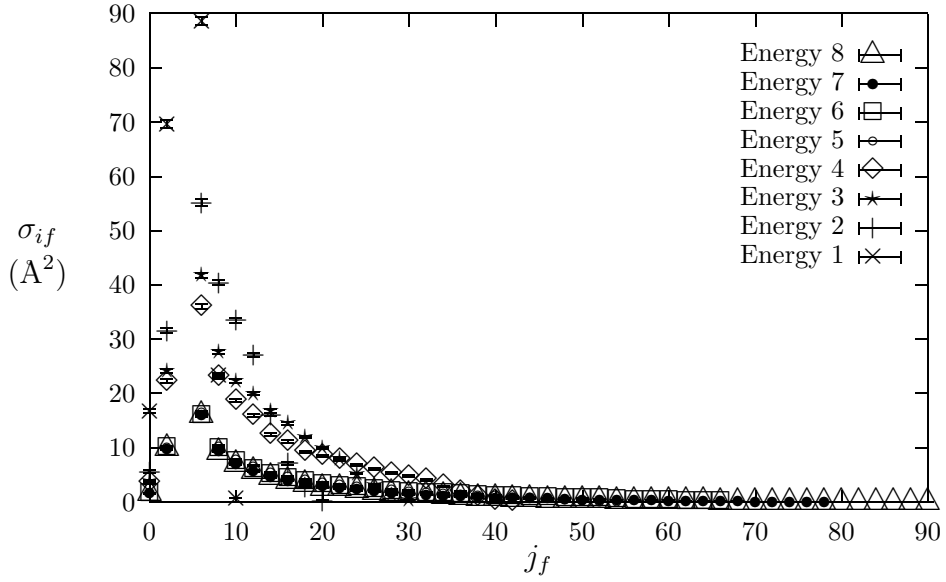

Figure 3.5: Classically computed cross sections for $\Delta v = 0$.

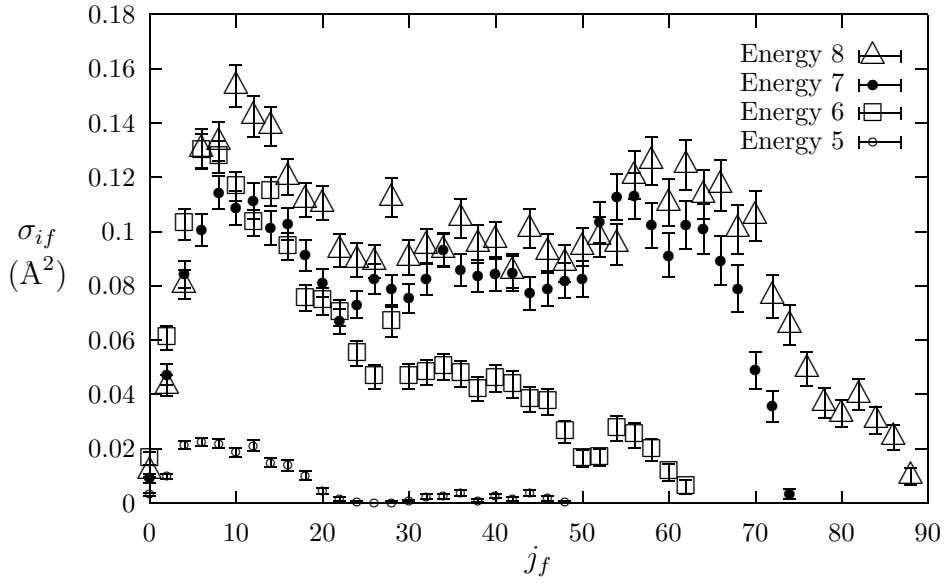

Figure 3.6: Classically computed cross sections for $\Delta v = 1$. In the classical calculations, the $\Delta v = 1$ vibrational level is only accessible at the highest four of the eight included Gauss-Laguerre energies.

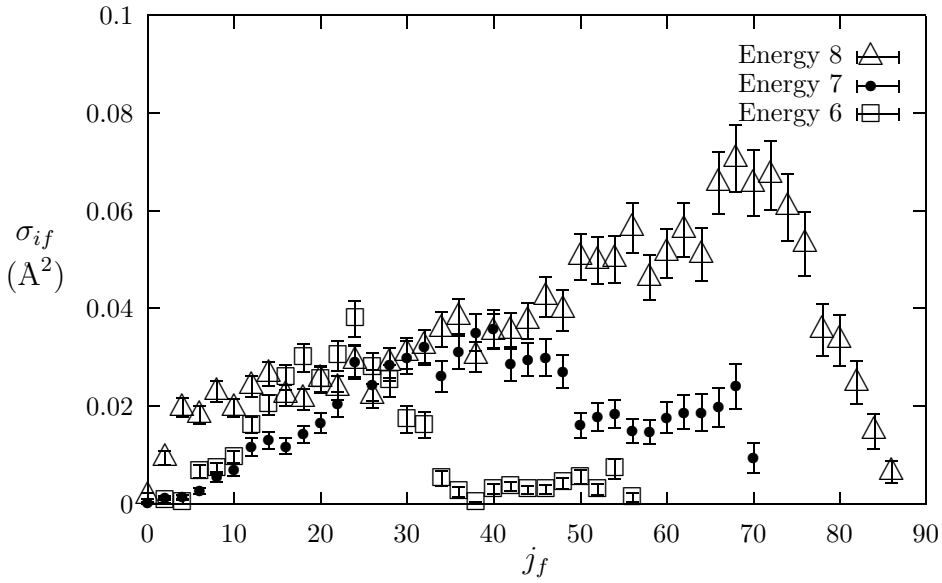

Figure 3.7: Classically computed cross sections for $\Delta v = 2$. In the classical calculations, the $\Delta v = 2$ vibrational level is only accessible at the highest three of the eight included Gauss-Laguerre energies.

quantum mechanically computed, and classically computed rate constants is performed.

Chapter 4

Quantum Mechanics

In this chapter, I discuss how the theory of quantum physics can be applied to determine rate constants for vibrotationally inelastic atom-diatom collisions, and summarize my work in obtaining rate constants for ($v_i = 0$, $j_i = 4$) in Li_2 $A^1\Sigma_u^+ - Ne$ via quantum calculations run using a program called *Hibridon* [Hib].

The quantum mechanically computed rate constants constitute the hardest-won body of data presented in this thesis. Whereas the experiments were set up and run in a few weeks' time, and the classical calculations were completed easily in under two weeks with no intervention necessary, I spent several months gradually learning what I needed to know in order to use the *Hibridon* scattering package to compute the quantum mechanically correct rate constants for our system at the initial molecular vibrotational state ($v_i = 0, j_i = 4$) of interest. Therefore, I have devoted extra attention in this chapter to discussing the basis for the calculation method and to documenting what I have learned thus far regarding the necessary ingredients for a successful calculation, in the hope that study of this thesis will help others to continue this project in the future.

4.1 Basic Quantum Molecular Scattering Theory

The quantum mechanical calculations of the rate constants parallel the classical calculations in a few basic respects. In both cases, we begin with a potential energy surface $V(q_1, \ldots, q_N)$ that describes the unique properties of the atom-diatom system of interest – in this case, the Alexander-Werner Li_2 $A^1\Sigma_u^+ - Ne$ PES [AW91]. Given the PES, our main task is to numerically solve a set of coupled differential equations. Each calculation is run for a single collision speed, at which cross sections σ_{if} are computed. The cross sections from calculations run at various speeds are then integrated via the Gauss-Laguerre method to produce the thermally averaged rate constants $\bar{k}_{if}$ that we seek.

At roughly this point, however, the similarities end. Whereas in classical physics it is appropriate and perfectly correct to simulate individual collision trajectories, the theory of quantum mechanics tells us that particles at the molecular scale do not follow definite trajectories that obey equations of motion. Instead of solving Hamilton's equations or their equivalent to model the courses of individual collisions instant by instant, we are left to solve the Schrödinger equation

$$\left[-\frac{\hbar^2}{2m}\nabla^2 + V(q_1, \ldots, q_N)\right]\Psi(q_1, \ldots, q_N) = E\Psi(q_1, \ldots, q_N) \tag{4.1}$$

to find the wavefunctions Ψ and energy eigenvalues E that describe the possible states of the system.

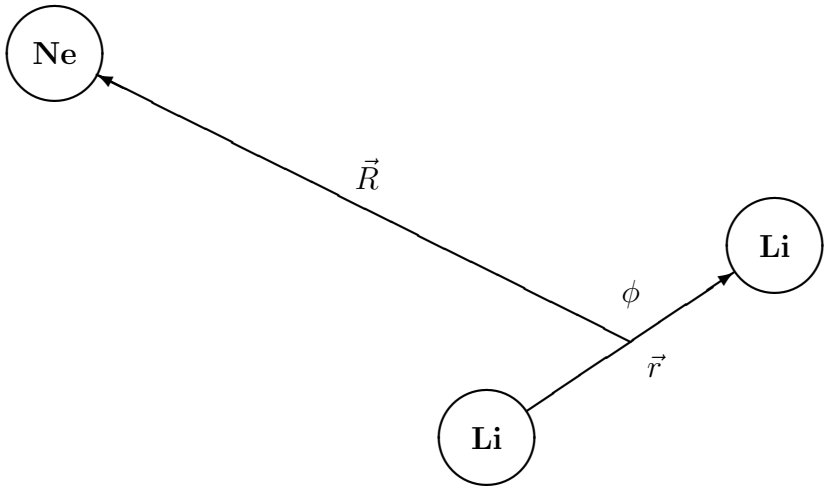

Figure 4.1: Coordinates of the $Li_2 - Ne$ system. $\vec{r}$ is the vector from one Li nucleus to the other, $\vec{R}$ is the vector from the molecule's center of mass to the atomic collision partner, and ϕ is the angle between $\vec{r}$ and $\vec{R}$. r and R denote the magnitudes of $\vec{r}$ and $\vec{R}$, respectively. The molecule's internal coordinates may be written as a vector $\vec{s} = (r, \phi)$.

4.1.1 The Coupled-Channel (CC) Equations

The task of directly solving the Schrödinger equation via many-dimensional numerical integration is exceedingly computationally intensive, so in practice one must always seek to simplify solution by reducing the number of variables involved. The standard method for doing this is to expand the system's wavefunctions in a known basis set. This trick makes it possible to reduce the Schrödinger equation to a coupled set of differential equations in $\vec{R}$ (see Fig. 4.1), known as the *multichannel equations*. Through the application of a partial wave expansion, the multichannel equations are further simplified to a coupled set of equations in the scalar atom-molecule separation coordinate R.

Two classes of basis are available for the first expansion. We may choose

a basis whose wavefunctions are functions of the molecule's internal coordinates $\vec{s} = (r, \phi)$ only (termed a *diabatic* basis), or a basis whose wavefunctions include a dependence on the atom-diatom separation coordinate R as well (referred to as an *adiabatic* basis). While the choice of an adiabatic basis makes computing the basis wavefunctions more difficult, this approach has the computational advantage of requiring the inclusion of fewer basis functions to obtain a desired degree of precision, and it is the approach taken by the program we used to obtain our quantum mechanical rate constants [HibDoc].

Our system's Hamiltonian can be written as a sum of three terms

$$H = \underbrace{-\frac{\hbar^2}{2\mu}\nabla^2(\vec{R})}_{\text{relative CM motion}} + \underbrace{V(R,\vec{s})}_{\text{interaction potential}} + \underbrace{H_0(\vec{s})}_{\text{internal motion of molecule}} . \qquad (4.2)$$

The first term accounts for the kinetic energy of the atom and diatom's translational motion relative to one another. The last term accounts for the molecule's internal motions (vibration and rotation). The middle term $V(R, \vec{s})$ specifies the energy associated with the mutual interaction of the atom and diatom. It is dependent on both the distance R between the collision partners and the relative spatial orientation and internuclear separation $\vec{s}$ of the molecule. As R gets very large, the interaction term becomes negligible. This is the region in which we are interested in the solution – the so-called *asymptotic* region, in which the collision partners have interacted and exchanged energy and are now flying apart as free particles. From the asymptotic region solutions we can obtain the total scattering cross sections σ_{if} that tell us about the possible post-collision states of the molecule and their associated probabilities for the total collision energy (sum of kinetic, vibrational, and rotational) in question.

In solving for the scattering wavefunctions, the adiabatic basis is chosen

to be the eigenfunctions $\Lambda_j(R,\vec{s})$ of $V(R,\vec{s})+H^0(\vec{s})$. The expanded wavefunctions $\Psi(\vec{R},\vec{s})$ of the atom-molecule system are then written as

$$\Psi(\vec{R},\vec{s})=\sum_j \psi_j(\vec{R})\ \Lambda_j(R,\vec{s}). \tag{4.3}$$

Substituting this form into the Schrödinger equation for the colliding system, where Eq. 4.2 is the system's Hamiltonian, premultiplying by a basis eigenfunction $\Lambda_j(R,\vec{s})$, and integrating over the internal coordinates $\vec{s}$ yields the multichannel equations [MB89]

$$\left[-\frac{\hbar^2}{2\mu}\nabla^2(\vec{R})+E_i(R)-E\right]\psi_i(\vec{R})-\frac{\hbar^2}{2\mu}\sum_j\left[\nabla^2_{ij}+2\nabla_{ij}\nabla(\vec{R})\right]\psi_j(\vec{R})=0 \tag{4.4}$$

where the $E_i(R)$ are the energies associated with the basis functions $\Lambda_i(R,\vec{s})$, and

$$\nabla^2_{ij}=\langle\Lambda_i(R,\vec{s})|\nabla^2(\vec{R})|\Lambda_j(R,\vec{s})\rangle \tag{4.5}$$

are the matrix elements of the kinetic energy operator for the relative motion of the atom and molecule.

In practice, it is necessary to truncate the expansion (4.3) of $\Psi(\vec{R},\vec{s})$ at some finite number of terms. The resultant set of coupled equations are called the *close-coupled* or *coupled-channel* (CC) equations. This is the system of equations that is solved to find final state cross sections in an exact quantum mechanical treatment.

Once we have the CC equations, we are left with the task of obtaining accurate numerical solutions. This task in itself is sufficiently difficult that some kind of approximate integration method is called for. Two classes of approximation method have traditionally been applied at this stage [HibDoc]: *solution-following* methods, in which the solution is approximated but the exact form of

the potential is used, and *potential-following* methods, in which an exact solution to an approximation of the potential is sought. Each class of method has its advantages and drawbacks in terms of computational accuracy. Solution-following methods work better at small values of the internuclear separation coordinate r, where the potential varies rapidly, while potential-following methods produce better results at large values of r, where the potential does not vary as rapidly but the solutions may be highly oscillatory. For this reason it is desirable to employ a hybrid integration scheme in which the range of integration is split and each of the two methods is applied in the region to which it is best suited. This is the approach taken by the *Hibridon* program, which employs a solution-following method (the log-derivative method of Johnson [Jo73, Jo79], Secrest [MS83], and Manolopoulos [Ma86]) at small r, and a potential-following method (the Airy propagator of Gordon [Gd69, Gd71], Alexander [Al84, AM87], and Manolopoulos [AM87]) at large r.

4.1.2 Computational Demands of the Quantum Calculations

It would seem at this stage that we have already introduced a good number of simplifications and approximations. Yet our problem still presents a major computational challenge. Solution of the CC equations is impractical, it turns out, for many of the higher energies that are necessary for a precise determination of the rate constants. To understand the nature of this limitation, we must look at the major factors that determine the computation time.

The time required to solve the CC equations is proportional to the cube of the number of channels N that must be included in the calculation, where the

term *channel* refers to a possible post-collision state of the molecule, with some particular (v, j) and angular momentum projection quantum number m.[1] N is in turn a function of the *total energy* of the collision. That is, it is a function of the sum of the kinetic energy of the atom and diatom's relative motion and the energy associated with the molecule's vibration and rotation before the collision:

$$E_{\text{total}} = E_{\text{relative motion}} + E_{\text{vib}} + E_{\text{rot}}. \tag{4.6}$$

The total collision energy is important because, being a conserved quantity, it determines which final states of the molecule will be accessible. Specifically, if we want to find out the highest vibrational and rotational state accessible via collisional energy transfer, we can imagine the most favorable case, in which essentially all of the available total energy goes into vibration and rotation, and the collision partners are left with practically no kinetic energy of relative motion afterward (they are moving apart very slowly).[2] Since the vibrational component of the energy is approximately $(v + \frac{1}{2})\hbar\omega$ (the energy of a quantum mechanical harmonic oscillator), the highest accessible vibrational state is approximately that specified by the largest integer v_{max} less than or equal to

$$\frac{E_{\text{total}}}{\hbar\omega} - \frac{1}{2}. \tag{4.7}$$

(In reality, the r-dependent part of the molecular potential is not a harmonic oscillator potential, so Eq. 4.7 is not an exact expression, but the approximation

[1] As mentioned later in this section, the rotational levels are degenerate, meaning there are many rotational states that share the same energy. The quantum number m is the additional quantum number that is required to specify which rotational *state* within a rotational *level* j is meant.

[2] Since the vibrational and rotational states have discrete energies, there may be some energy left over that is not sufficient to add another unit of vibration or rotation. This remaining energy takes the form of translational kinetic energy, giving the collision partners some relative speed after the collision, since there is nowhere else for it to go.

is a good one for small v, and is adequate for the point being made here.) Within each accessible vibrational state $0 \ldots v_{\max}$, we can find the highest accessible rotational state by taking the remaining energy

$$E_{\text{remaining}} = E_{\text{total}} - E_{\text{vib}} = E_{\text{total}} - (v + \frac{1}{2})\hbar\omega \tag{4.8}$$

and seeing how high this can take us in j. Unlike vibrational state energies, rotational state energies are not evenly spaced, so we can't write down a simple formula such as Eq. 4.7 for $j_{\max}$. However, the idea is simple enough. The energy of rotation for a given j is essentially the quantum mechanical rigid rotor energy $E_{\text{rot}} = Bj(j+1)$, but because the molecule's vibration influences its rotation (classically, by varying the length of the 'rotor' and hence its moment of inertia) we must include higher order correction terms as well. Usually it is adequate to stop at the third order term in $j(j+1)$, giving

$$E_{\text{rot}} = Bj(j+1) - D[j(j+1)]^2 + H[j(j+1)]^3 \tag{4.9}$$

where the *rotational constant* B and the *centrifugal distortion coefficients* D and H vary slightly with v. To find $j_{\max}$ for a given v, we simply seek the largest j for which $E_{\text{rot}} \leq E_{\text{remaining}}$ with $E_{\text{remaining}}$ as in Eq. 4.8. (Table 4.1 lists E_{vib} and the rotational coefficients B, D, and H for $v = 0 - 4$ in $Li_2 A^1\Sigma_u^+$ to illustrate the scale of energies involved in vibration and rotation. Comparison of B and ΔE_{vib} shows that the rotational levels are much more closely spaced than the vibrational levels.)

Now that we know how to find out which post-collision levels are accessible, we should be able to count the number N of channels (post-collision states). The rotational states of the molecule, like those of a rigid rotor, carry a

v	$E_{\rm vib}$	$\Delta E_{\rm vib}$	B	D	H
0	0	-	0.494688	7.43607e-6	9.66872e-11
1	252.31	252.31	0.489247	7.37208e-6	9.50437e-11
2	501.49	249.18	0.483845	7.30967e-6	9.34002e-11
3	747.55	246.06	0.478479	7.24901e-6	9.17568e-11
4	990.51	242.96	0.473148	7.19026e-6	9.01133e-11

Table 4.1: Vibrational energies $E_{\rm vib}$ and rotational coefficients B, D, H for $v = 0 - 4$ in Li_2 $A^1\Sigma_u^+$. $\Delta E_{\rm vib}$ indicates the local energy spacing between vibrational levels. The small variation of $\Delta E_{\rm vib}$ and the rotational coefficients with v is due to vibration-rotation coupling. All energies and coefficients are listed in $\rm cm^{-1}$.

$2j + 1$ degeneracy. (There are $2j + 1$ distinct states that share the same energy level.) Hence the number of rotational states accessible in some v with a given $j_{\rm max}$ is

$$N_{\rm rot} = \sum_{j=0}^{j_{\rm max}} (2j + 1) = (j_{\rm max} + 1)^2 \tag{4.10}$$

which essentially goes as $j_{\rm max}^2$. Accounting for vibration, we find that the number of open channels in a CC calculation is

$$N = \sum_{v=0}^{v_{\rm max}} \sum_{j=0}^{j_{\rm max}(v)} (2j + 1) = \sum_{v=0}^{v_{\rm max}} (j_{\rm max}(v) + 1)^2. \tag{4.11}$$

When we consider that even for a calculation that only includes one vibrational level the time complexity goes as $O(N^3) \sim O([j_{\rm max}^2]^3) = O(j_{\rm max}^6)$ it becomes clear that the computer time required to solve an atom-diatom scattering problem increases rapidly without limit as more accessible levels are added. As illustrated by the computational results presented in the section to follow, the CC calculations include so many channels as to be impractical for the higher energies we need to include in our Gauss-Laguerre integration to calculate accurate rate constants. These calculations are pushing the limit of what can be done in a reasonable amount of time, even on the current crop of high-speed workstations.

A further simplification is needed if we are to obtain any results at all at these higher energies. A few different approximation methods have been historically applied to address this problem. The program we used for our calculations supports use of the *coupled state* (CS) approximation, in which averaging over orbital angular momenta decouples terms with different angular momenta, resulting in a simplification of the CC equations [MB89]. This reduces the number of channels involved in a calculation to $O(j_{\max})$, so that the computation time now goes as $O(j_{\max}^3)$ instead of $O(j_{\max}^6)$, which turns out to provide enough of a time savings to render calculations at our highest Gauss-Laguerre energies feasible.

4.2 Calculation of the Rate Constants

We calculated integral cross-sections for comparison with our empirically obtained rate constants using a program called *Hibridon* developed by Alexander *et. al.* [Hib], in conjunction with an accurate *ab initio* PES for Li_2 $A^1\Sigma_u^+ - Ne$ obtained by Alexander and Werner [AW91]. As with our classical calculations, we performed a Gauss-Laguerre integration of our cross sections over a sampling of energies to take into account the thermal and laser-selected distribution of collision speeds in our experiments. We used the same selection of collision energies as in the classical trajectory runs.

As explained earlier, the amount of time a calculation takes is proportional to N^3, where N is the number of channels required for the calculation. Table 4.2 shows the number of channels involved in cross section calculations at each of the eight Gauss-Laguerre collision energies when $v = 0 - 2$ are included. I began my project by attempting exact CC calculations, and soon found that

		$j_{\max}$ for $v = 0 - 4$					# of channels for $v = 0 - 2$	
#	E (cm^{-1})	$v = 0$	$v = 1$	$v = 2$	$v = 3$	$v = 4$	CC	CS
1	55.2027	14	-	-	-	-	64	8
2	249.1503	26	-	-	-	-	196	14
3	600.2090	38	30	16	-	-	737	45
4	1112.2166	50	44	38	30	18	1605	69
5	1790.9502	64	60	56	50	44	2891	93
6	2644.5274	78	76	72	68	64	4490	116
7	3684.0297	94	92	88	84	82	6538	140
8	4924.4478	110	108	106	102	100	9077	165

Table 4.2: Maximum accessible rotational levels and resultant number of channels involved in quantum calculations that include $v = 0 - 2$ at each of the eight sample energies. Note the rapid increase in the number of channels required for the CC calculations. The CS calculations require significantly fewer channels, due to removal of the $2j + 1$ rotational state degeneracy by decoupling of angular momenta in the CS treatment.

carrying these calculations beyond the third sample energy (600 cm^{-1}) would be impractical given the time available to me for this study. The $v = 0$, 1, and 2 CC calculations for the third energy took approximately 8 days to complete on our fastest workstation, a Silicon Graphics O_2, and the N^3 scaling rule indicates that 150 days would be needed to complete the like calculation for the fourth energy on the same machine. Cross sections calculated for the lowest three Gauss-Laguerre energies alone would not be sufficient to yield accurate rate constants, particularly for vibrationally inelastic collisions ($\Delta v \neq 0$), so we found we had to turn to the CS approximation. In collaboration with *Hibridon*'s primary author, Millard Alexander of the University of Maryland at College Park, I ran CS calculations including $v = 0 - 2$ for all eight energies, and CC calculations for the five lowest energies that were variously restricted in range of v.[3] (CC calculations were carried out up to and including the fifth energy for

[3]The first five of the $v = 0$ CC calculations have completed thus far; the sixth is still in

Calculation Type	Gauss-Laguerre Energy #	# of channels	CPU Time (HH:MM)
CC, v=0-2	1	64	0:01
	2	196	25:00
	3	737	192:06
CS, v=0-2	4	69	0:18
	5	93	0:50
	6	116	2:04
	7	140	5:32
	8	165	16:33

Table 4.3: Timings for calculations run on a Silicon Graphics O_2 workstation.

Calculation Type	Gauss-Laguerre Energy #	# of channels	CPU Time (HH:MM:SS)
CS, v=0-2	1	8	0:01:26
	2	14	0:01:58
	3	45	0:19:26

Table 4.4: Timings for calculations run on a Silicon Graphics Indy workstation.

$v = 0$, the fourth energy for $v = 1$, and the third energy for $v = 2$.)

We ran the calculations concurrently on a variety of workstations, so a straightforward comparison of computation times would not be meaningful. However, timings are given in Tables 4.3 and 4.4 for two of the machines used. In addition to taking time on the order of N^3 to complete, the calculations carry a memory requirement that goes as N^2. Because the computations are so slow to begin with, an added slowdown due to the use of virtual memory would be unacceptable. Hence a workstation must be equipped with sufficient memory for the calculations it is to run, placing a limit of approximately 1200 channels on the types of calculations that we could run.

progress. A CC calculation at the fourth energy that includes open vibrational channels is planned.

4.2.1 The Calculation Parameters

Table 4.5 lists the most important parameters supplied to a quantum cross section calculation at a given energy, along with synopses of their functions and typical values where appropriate. (A number of other parameters not listed here control output of results and diagnostics.) The parameters are grouped in six functional categories in Table 4.5. The parameter groups control the total collision energy, the numerical integration, the inclusion of partial waves, iteration over angular momentum, the inclusion of channels, and the calculation type (CC or CS). The following discussion of parameters elaborates on the summaries given in Table 4.5, highlighting key parameters by group.

In the second group, the parameters `rstart`, `rendld`, and `rendai` determine the range of r for which each integration method (log-derivative and Airy) will be applied, while `spac`, `fstfac`, `rincr`, and `tolai` control the integration step size. The endpoint for the whole integration, specified by `rendai`, is the main parameter among these that I adjust when checking for proper convergence of the cross sections. If the cross sections for a given run do not change appreciably when `rendai` is increased by a few Bohr, they are well converged with respect to this parameter. Similarly, if the cross sections do not change much when `rendai` is decreased slightly, then calculation time can be saved by reducing this value. I have not had cause to alter the values of the other integration parameters significantly.

Parameters `jtot1`, `jtot2`, `jtotd`, `jlpar`, `numin`, `numax`, and `nud` control stepping through total angular momentum (for the CC calculations), or orbital angular momentum (for the CS case). I found the maximum value of

Parameter	Synopsis	Typical Value
energy	Total collision energy (kinetic + vibrational + rotational).	-
rstart	Integration starting point.	3.1-5.0 Bohr
rendld	Boundary where LOGD integration stops and AIRY starts.	6.5-7.5 Bohr
rendai	Integration ending point.	25.0 Bohr
spac	Step size for LOGD integration.	0.005-0.025 Bohr
fstfac	Starting step size for AIRY integration as a multiple of SPAC.	6.0
rincr	Value of r at which AIRY step size begins to change.	= rendld
tolai	If ≥ 1, factor by which step size changes at each step for $r > rincr$. If < 1, controls AIRY step size changes by error estimation method of Alexander [Al84].	1.040
jtot1	Initial value of total (CC) or orbital (CS) angular momentum.	0
jtot2	Final value of total (CC) or orbital (CS) angular momentum.	60-350
jtotd	Step size for total (CC) or orbital (CS) angular momentum.	2 (CC), 3-8 (CS)
jlpar	Selects parity of included channels.	0 (CC), 1 (CS)
rcut	Controls dropping of channels deemed unnecessary at high J_{tot}. Setting rcut = rendai disables channel dropping.	= rendai
numin	Minimum value of angular momentum projection index for CS calculations.	0
numax	Maximum value of angular momentum projection index for CS calculations.	4
nud	Step size for angular momentum projection index for CS calculations.	1
vmin	Minimum vibrational level to include.	-
vmax	Maximum vibrational level to include.	-
jmin	Minimum rotational level to include for each v included.	0
jmax	Maximum rotational level to include for each v included.	-
evib	Vibrational energy for each v included.	-
brot, drot, hrot	Rotational coefficients B,D,H for each v included.	-
csflag	True requests CS calculation, false does a CC calculation.	-
ihomo	True if the molecule is homonuclear (Li_2 certainly is).	True

Table 4.5: Main parameters for CC and CS quantum cross section calculations. Typical values are given where appropriate, to give some idea of appropriate ranges. These are based on settings I used for my calculations. The *Hibridon* documentation discusses these parameters and others in detail.

the total/orbital angular momentum, set by `jtot2`, to play a very important role in determining cross section convergence. In general, as the total collision energy is increased, `jtot2` must be increased to include contributions from more partial waves in order to obtain converged cross sections. I also found that the value of `jtot2` has a very significant effect on the calculation time. In a cross section calculation at a given total energy, *Hibridon* iterates through $J_{\mathrm{tot}} =$ `jtot1`$, \ldots,$ `jtot2` in increments of `jtotd`, performing integration over `rstart` to `rendai` at each step. The amount of time such a step takes increases rapidly with J_{tot}, so it is desirable to keep `jtot2` as small as is possible without affecting the cross sections appreciably. This seems to be a parameter one just has to experiment with, trying informed guesses based on cumulative experience. The step size parameter, `jtotd`, is set differently for CC and CS calculations. In the CC case, it is desirable to set `jtotd` = 2, causing *Hibridon* to step through first even J_{tot}, then odd J_{tot}, in the range `jtot1` to `jtot2`. For CS calculations, `jtotd` can be safely increased, which saves calculation time as one goes to higher total energies and increases `jtot2` to compensate.

The parameter `rcut` controls a criterion *Hibridon* uses to identify channels whose contributions become negligible at high J_{tot} and drop them from a calculation to save time. I have not yet ventured to make use of this feature; it may prove invaluable, however, as we push our calculations to higher total energies.

`jlpar` is a 'parity' control that is simply set to 0 for CC calculations and 1 for CS calculations.

The range of rotational levels to be included is determined for each v by `jmin` and `jmax`. To achieve good convergence of the cross sections, I have

found it necessary to include one or two closed rotational levels at each v. For instance, if I determine that, at some particular total collision energy, $j = 16$ is the highest open (accessible) rotational level in $v = 1$, I will typically set `jmax` = 18.

`vmin` and `vmax` control the inclusion of vibrational states. The initial state v_i must of course be included, as well as any vibrational states for which we wish to obtain cross sections. Unlike the case of rotational levels, it seems unnecessary to include closed vibrational states in a calculation, for both the CC and CS cases.

4.2.2 Choosing Appropriate Parameter Values

As illustrated in the previous section, the numerical solution of the CC and CS equations is controlled by a number of parameters, which have various effects on the convergence of the cross-section calculations. The primary challenge I encountered in this project was that of determining appropriate values for these parameters for each calculation. The selection of parameter values was problematic for a number of reasons.

First, an at least rudimentary background in quantum molecular scattering theory is necessary. The stronger this background, the more insight one has into how changing a given parameter is likely to affect the accuracy of the resultant cross-sections. The discussion contained in this chapter essentially represents the current extent of my knowledge in this area, which I acquired gradually over the past year, in the course of pursuing the calculation of rate constants I needed for the comparison presented in this thesis. Only now am I beginning to feel somewhat competent at selecting appropriate calculation parameters. I have

attempted herein to document as much as possible of the practical knowledge I have gained about this process, to help others in our group to continue these calculations in the future.

Even with a rudimentary grasp of the calculation parameters and their significance in hand, the problem of determining proper values for the parameters is not a trivial one. Enough variables are involved in determining the precision of the computed cross-sections that experimentation with variations in the parameter settings is the only practical way for someone without an extensive understanding of the theory to determine appropriate values. The problem with this approach is that the CC calculations are so time-consuming for higher energies that the practice of repeating the runs and iteratively adjusting parameters to check their effects on convergence of the cross sections is out of the question. While this process is practical at lower energies, where fewer channels are open and the calculations are faster, I have found no straightforward way to extrapolate from the low-energy CC parameters what parameter values will be sufficient for CC calculations at higher energies. And again, because the high-energy calculations are already pushing the limit of what we can do on a present-day workstation, there is little room for computational waste. Simply choosing cautious parameters all around (a large range of integration, small integration step size, inclusion of several closed channels, etc.) is not an option, because many of the parameters have significant effects on the already large calculation time.

Fortunately, it seems to be the case that parameters that prove adequate in CS calculations work reasonably well for the corresponding CC runs. A file of input parameters from a CS calculation can be readily converted to perform

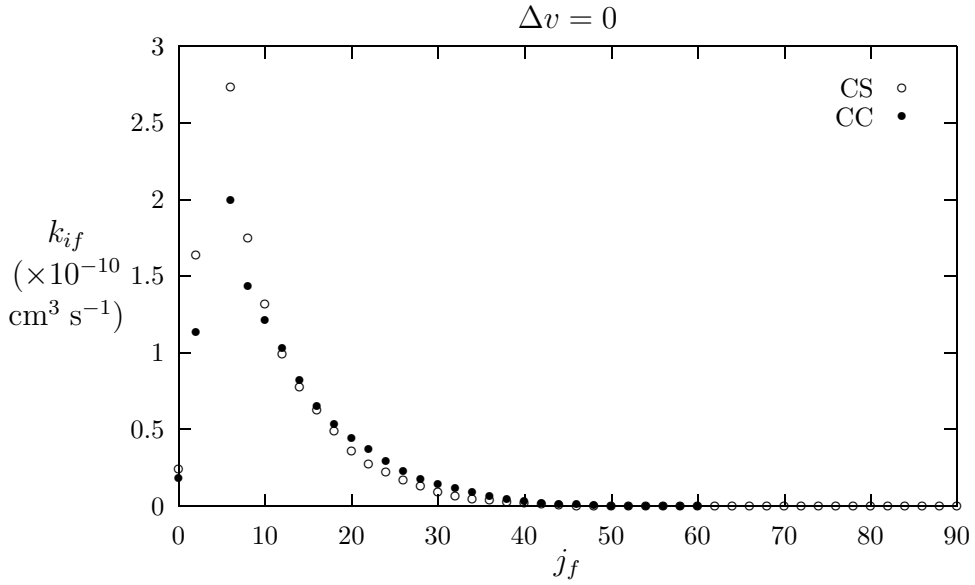

Figure 4.2: Thermally averaged rate constants for $\Delta v = 0$ computed via the coupled states (CS) approximation and by exact solution of the coupled channel (CC) equations. The CC calculations for $\Delta v = 0$ have been completed only up to the fifth energy (1791 cm^{-1}), so *only the first five terms* in the Gauss-Laguerre integration were taken in computing the $\Delta v = 0$ CC results.

the corresponding CC calculation by simply setting `csflag` = false, `jlpar` = 0, and `jtotd` = 2, typically with good results. Once this guideline was established, I had a considerably easier time with running CC calculations.

4.3 Results

The rate constants I obtained via the quantum mechanical CS and CC calculations are plotted in Figs. 4.2-4.4. The numerical values of the quantum mechanically computed rate constants are given in Appendix A.

The overall shape of the $\Delta v = 0$ rate constant distribution (Fig. 4.2) matches what we have come to expect from the experimental and classical results. There is also generally good agreement between the CC and CS results

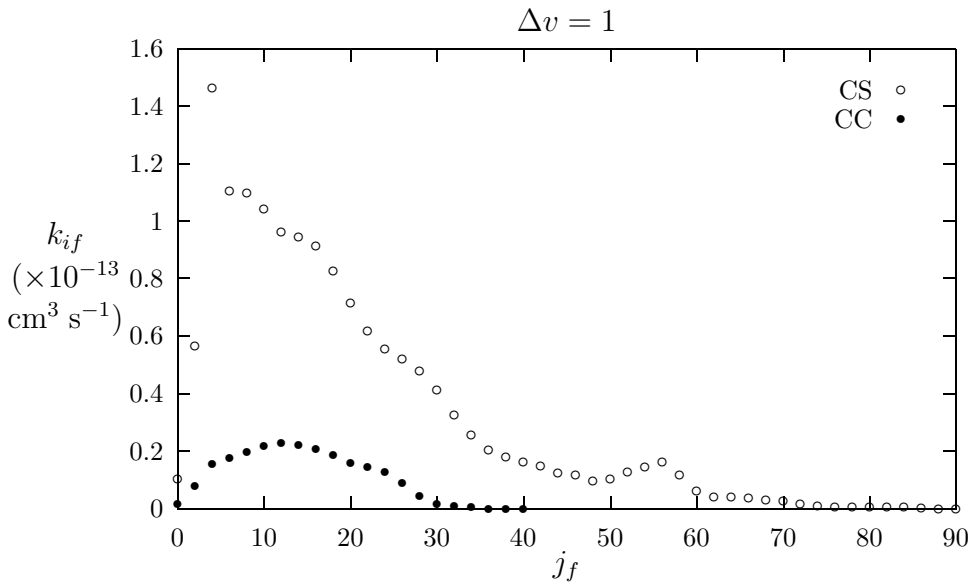

Figure 4.3: Thermally averaged rate constants for $\Delta v = 1$ computed via the coupled states (CS) approximation and by exact solution of the coupled channel (CC) equations. The CC calculations for $\Delta v = 1$ were run only up to the fourth energy (1112 cm^{-1}), so *only the first four terms* in the Gauss-Laguerre integration were taken in computing the $\Delta v = 1$ CC results.

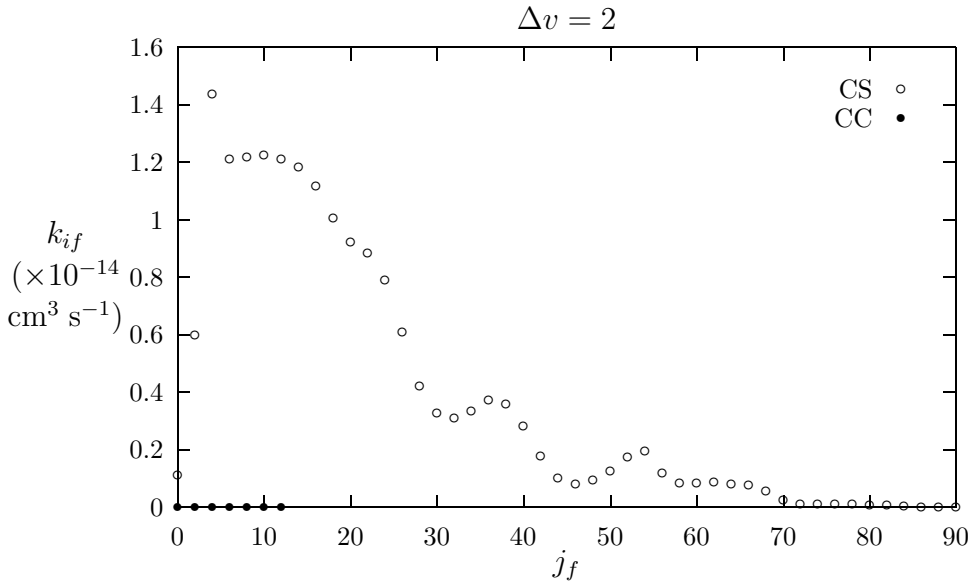

Figure 4.4: Thermally averaged rate constants for $\Delta v = 2$ computed via the coupled states (CS) approximation. The CC calculations for $\Delta v = 2$ have been completed only up to the third energy (600 cm^{-1}), so *only the first three terms* in the Gauss-Laguerre integration were taken in computing the $\Delta v = 2$ CC results, which are essentially negligible because $v_f = 2$ is only open at the third energy.

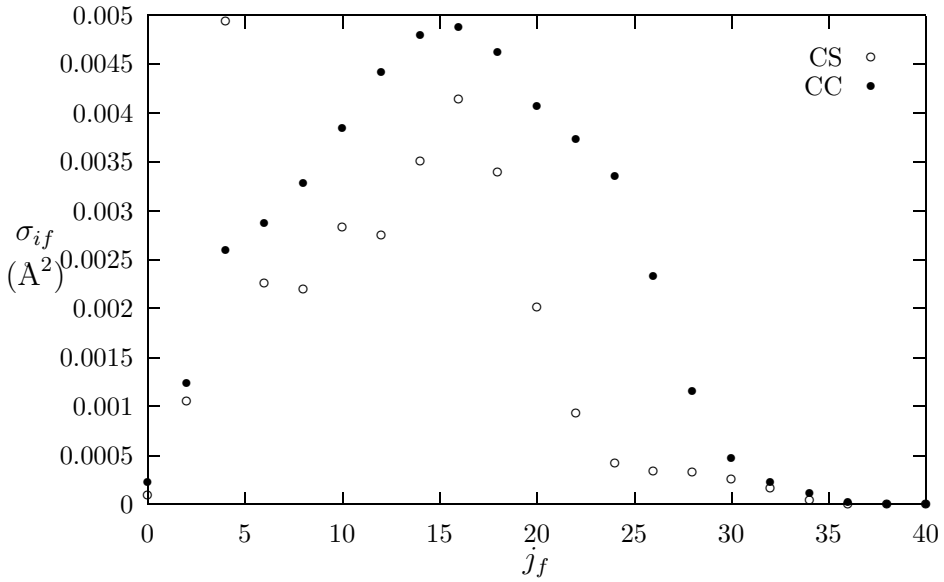

Figure 4.5: Comparison of CS and CC cross sections for $\Delta v = 1$, calculated at energy 4.

here, despite the fact that CC cross sections were not available for the three highest Gauss-Laguerre energies and hence had to be omitted from the CC rate constants.

At $\Delta v = 1$ and $\Delta v = 2$, however, there is clear disagreement between the CC and CS rate constants (see Figs. 4.3 and 4.4). In part, this is due to the omission of still more energies from the CC calculations (the $\Delta v = 1$ rate constants are based on energies 1-4, and the $\Delta v = 2$ rate constants include only energies 1-3), but I suspect that the results would still differ were it not for the omissions, based on differences in the CC and CS cross sections for energies where both were computed (see, for example, Fig. 4.5).

We also see bumpiness in the $\Delta v = 1$ and $\Delta v = 2$ rate constants similar to what was observed in the vibrationally inelastic classical calculations. Here again, the effect is due in part to the differing peak positions in the cross section

contributions from each energy (as illustrated in Figs. 4.8-4.11) and in part to the small number of terms in the Gauss-Laguerre integration. However, the evidence for a bimodal distribution is not as strong in the quantum cross sections as it is in the classical case (see Fig. 4.8).

The CC and CS quantum rate constants are examined further in the context of the three-way comparison presented in the next chapter.

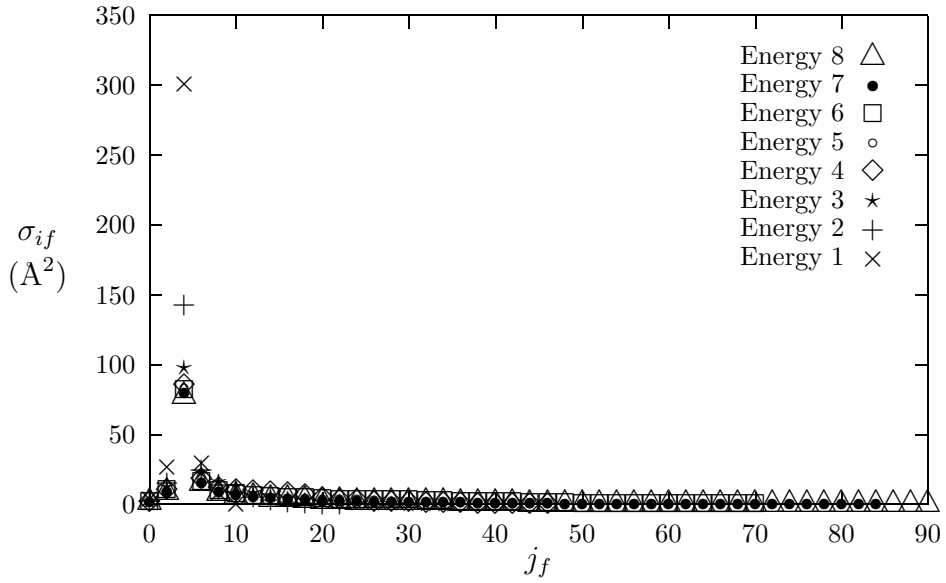

Figure 4.6: Cross sections for $\Delta v = 0$ computed via the coupled states (CS) approximation.

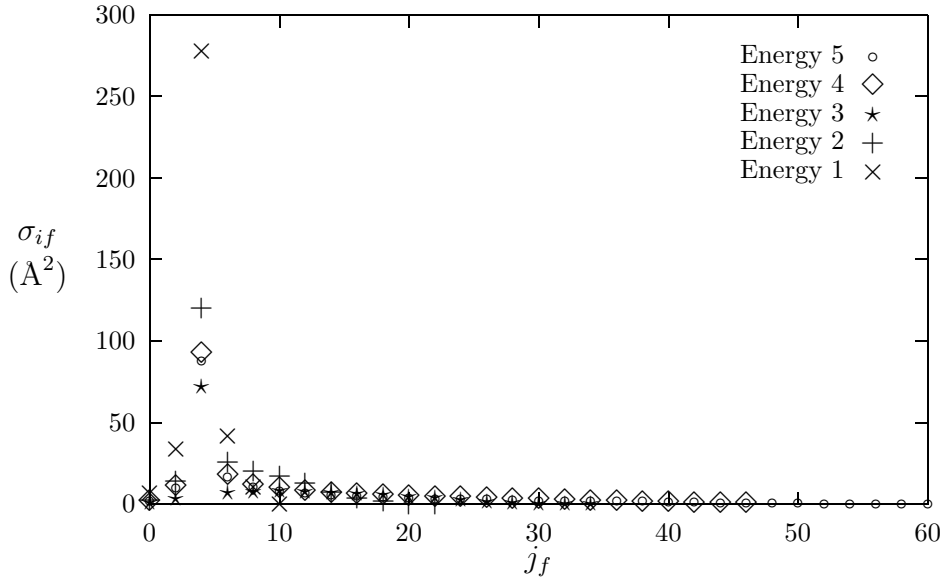

Figure 4.7: Cross sections for $\Delta v = 0$ computed via solution of the exact close coupled (CC) equations.

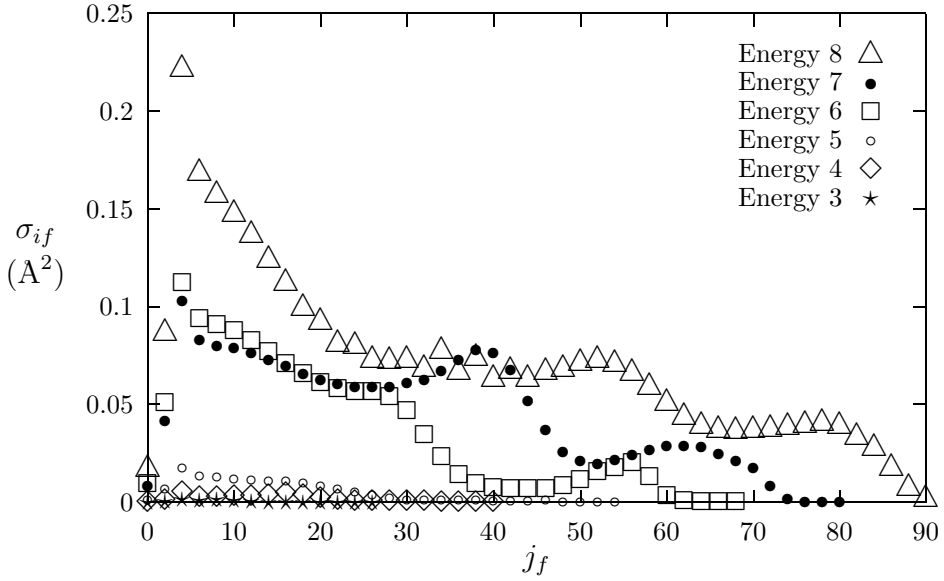

Figure 4.8: Cross sections for $\Delta v = 1$ computed via the coupled states (CS) approximation.

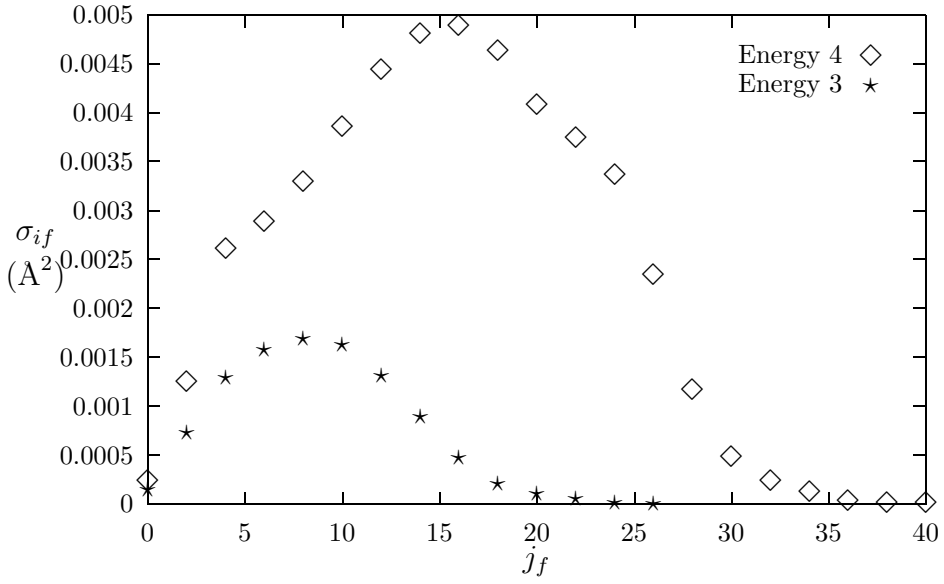

Figure 4.9: Cross sections for $\Delta v = 1$ computed via solution of the exact close coupled (CC) equations.

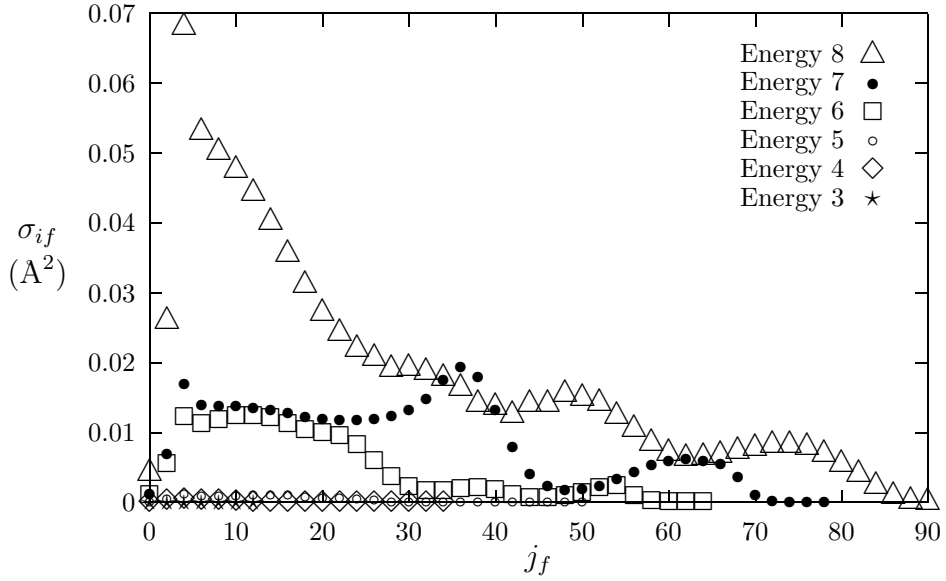

Figure 4.10: Cross sections for $\Delta v = 2$ computed via the coupled states (CS) approximation.

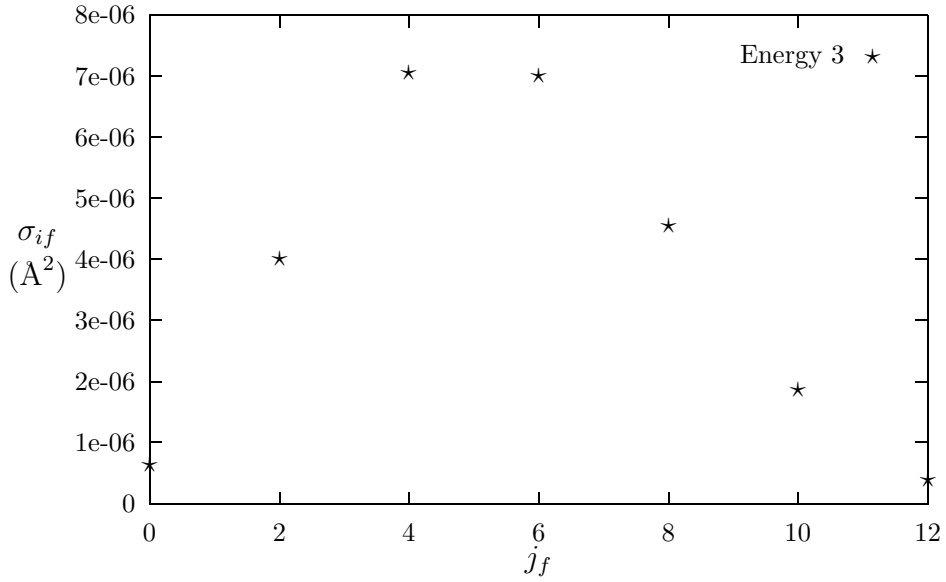

Figure 4.11: Cross sections for $\Delta v = 2$ computed via solution of the exact close coupled (CC) equations.

Chapter 5

Findings

In this chapter, I present a comparison among the experimentally obtained, quantum mechanically computed, and classically computed rate constants for $(v_i = 0, j_i = 4)$ in Li_2 $A^1\Sigma_u^+ - Ne$, and discuss interesting features of the results and their possible significance.

5.1 Observations by Final Vibrational Level

5.1.1 $\Delta v = 0$

Comparative plots of the $\Delta v = 0$ rate constants are shown in Figs. 5.1 and 5.2. These graphs alone are rich with interesting features.

To begin, we may note that there is generally good correspondence among all the vibrationally elastic results. The classical prediction of the $\Delta v = 0$ rate constants is conspicuously too large for $j_f \leq 20$, where the experimental rate constants are more closely fitted by the quantum CC and CS results, but the classical results are at least reasonable in order of magnitude.

A curious feature of the vibrationally elastic rate constants revealed in Fig. 5.2 is that the experimental data appear to be more closely fit by the

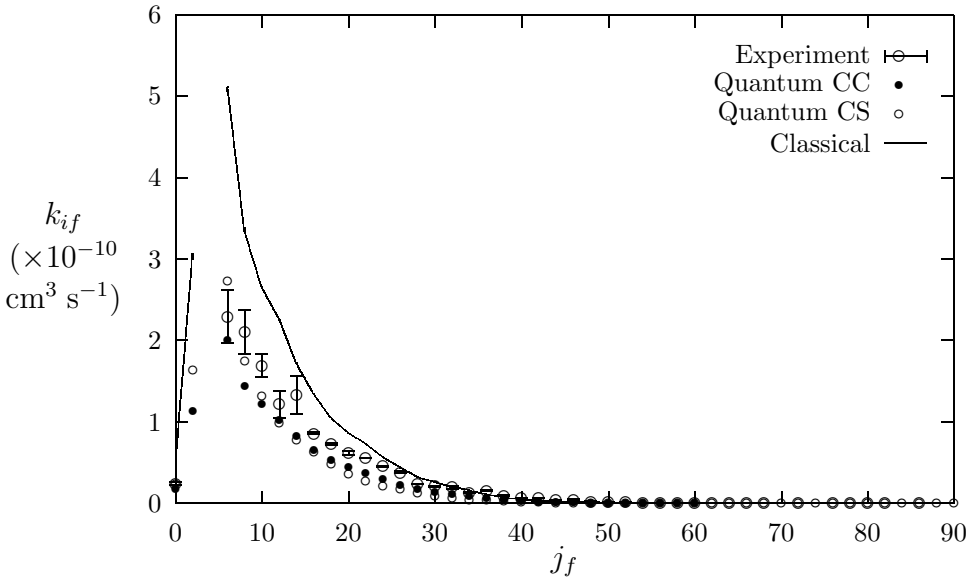

Figure 5.1: Linear-scale comparison of the thermally averaged rate constants for $\Delta v = 0$

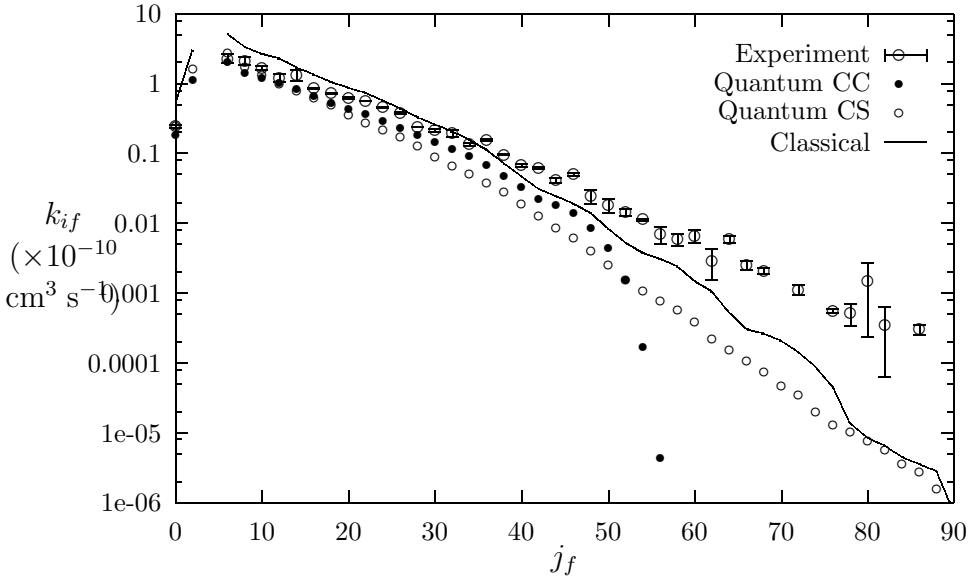

Figure 5.2: Semilog-scale comparison of the thermally averaged rate constants for $\Delta v = 0$

classically computed rate constants than by either of the quantum calculations for $36 \leq j_f \leq 50$. We cannot say with any certainty what the case for the CC quantum calculations would be at $j_f > 50$, since there is a marked artificial dropoff in the CC rate constants beginning at this point, due to the fact that CC calculations including $v = 0$ have only been completed through the fifth Gauss-Laguerre energy as of this writing. However, the CS rate constants remain smaller than their classical counterparts out to $j_f = 88$, and both these sets of results appear to be slowly diverging from the empirical rate constants as j_f increases.

5.1.2 $\Delta v = 1$

Figs. 5.3 and 5.4 show the comparative values of the rate constants for $\Delta v = 1$. The agreement between the empirical and the computational results is clearly poor in this case, with neither the classical nor the CS rate constant distributions showing similarity to the empirical values in either peak position or overall magnitude.

The CC rate constants for $\Delta v = 1$ suffer from the absence of one more contributing energy than do those for $\Delta v = 0$, being determined from CC cross sections calculated at the four lowest energies only. As a result, they not only contain a sharp artificial falloff beginning around $j_f = 26$, but are smaller than the CS results by a factor of about 10. The latter effect is not surprising because the higher collision energies have contributions to make to transfers of $\Delta v = 1$, even for small Δj, which should be significant in spite of the small values of the Gauss-Laguerre weights for the highest energies.

Due to the significant amount of information missing from the CC rate

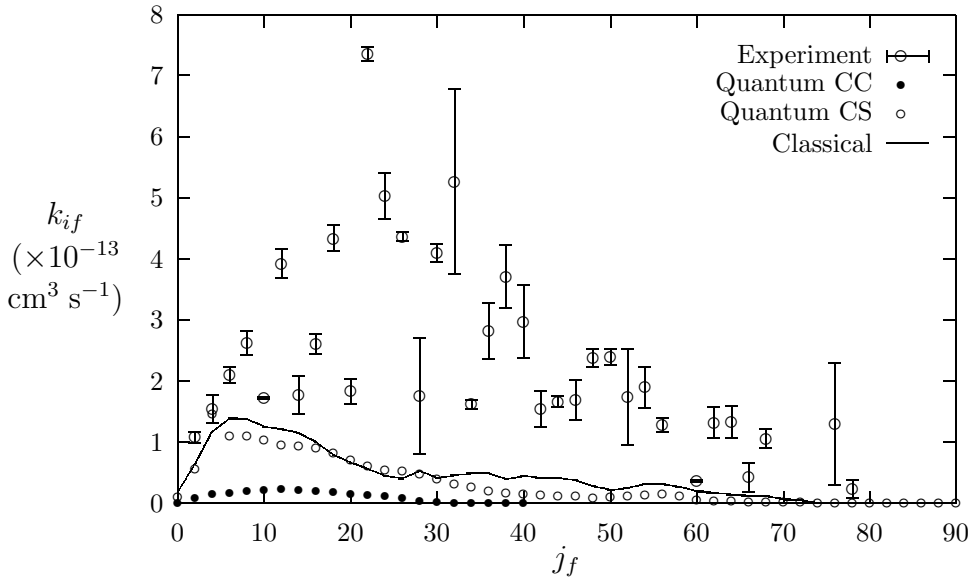

Figure 5.3: Linear-scale comparison of the thermally averaged rate constants for $\Delta v = 1$

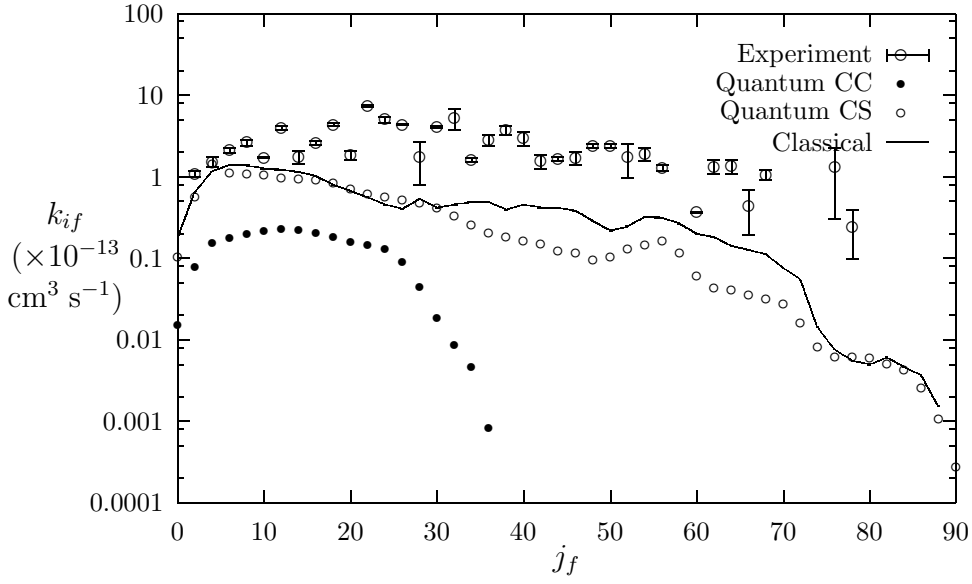

Figure 5.4: Semilog-scale comparison of the thermally averaged rate constants for $\Delta v = 1$

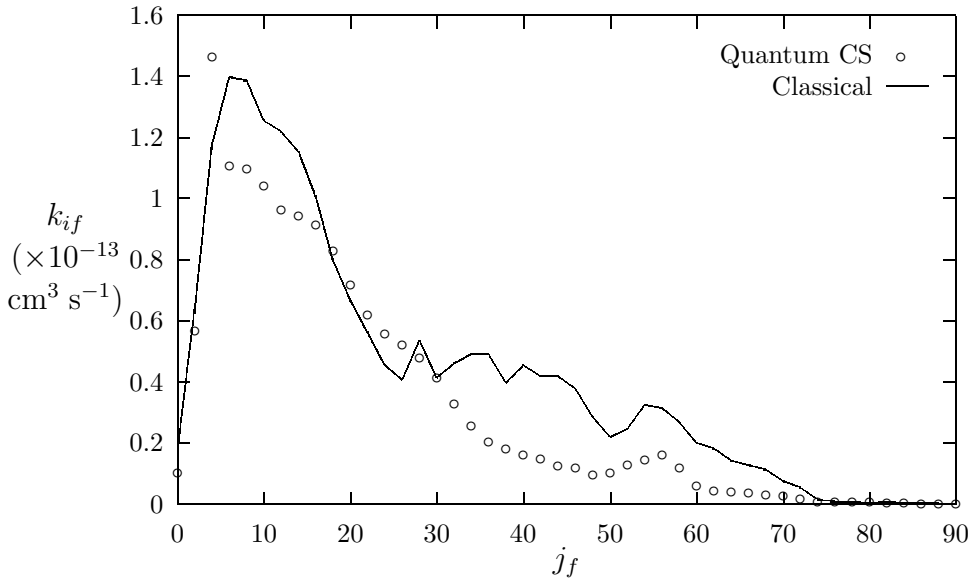

Figure 5.5: Linear-scale comparison of the thermally averaged rate constants computed via the CS quantum and classical methods for $\Delta v = 1$

constants for $\Delta v = 1$, we can only meaningfully compare the CS and classical results with the experimental rate constants in this case. While neither of these models fits the experimental figures well, the CS quantum results are further from the empirical values in the region $32 \leq j_f \leq 72$ than are the classical, as occurred in the $\Delta v = 0$ rate constants for $22 \leq j_f \leq 76$. Both models agree, however, on the general location of the peak in the $\Delta v = 1$ distribution, placing it near $j_f = 6$ or 8 (see Fig. 5.5) – whereas the empirical rate constants seem to peak closer to $j_f = 20$.

5.1.3 $\Delta v = 2$

Figs. 5.6 and 5.7 show the rate constants for $\Delta v = 2$. As noted in Chapter 2, the experimental rate constants in this vibrational manifold do not exhibit a clearly defined pattern.

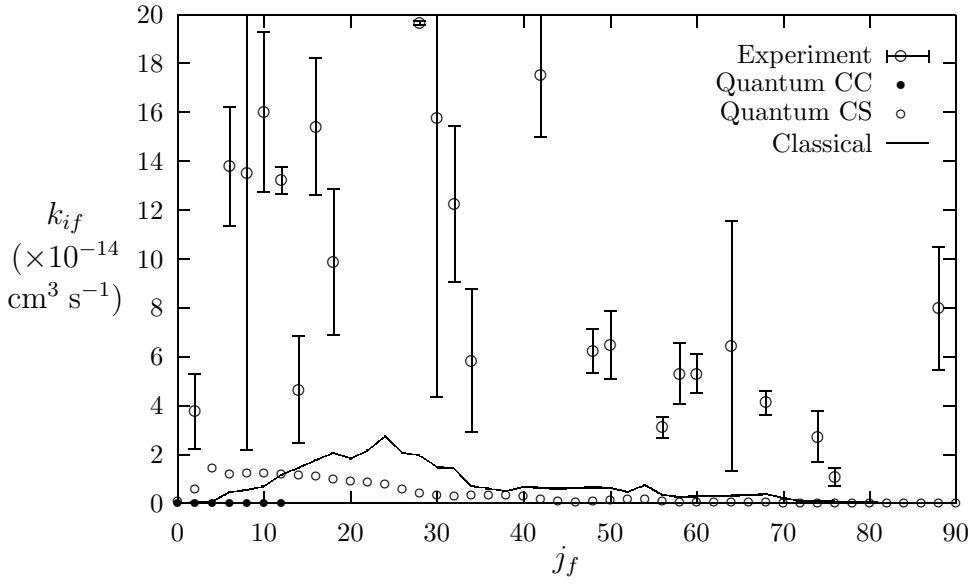

Figure 5.6: Linear-scale comparison of the thermally averaged rate constants for $\Delta v = 2$

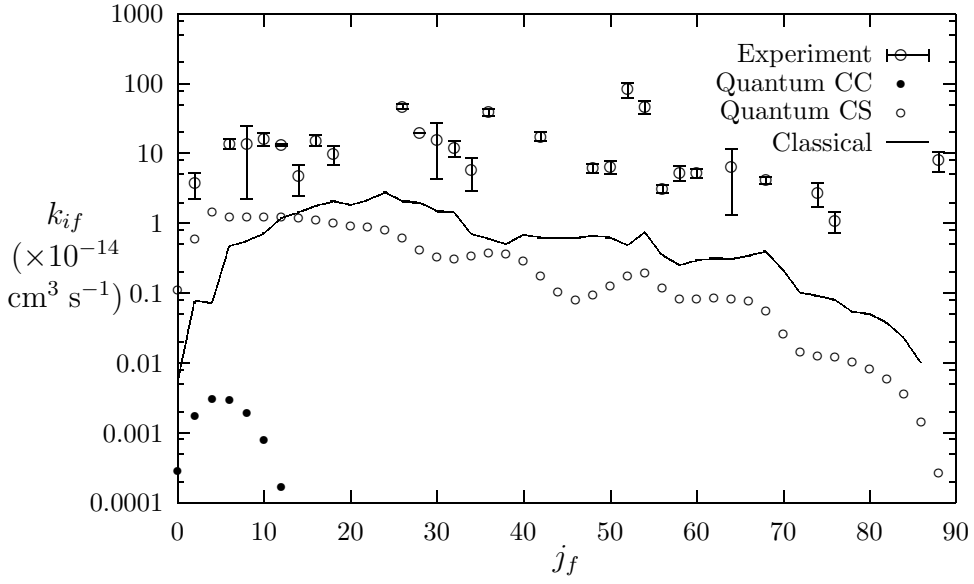

Figure 5.7: Semilog-scale comparison of the thermally averaged rate constants for $\Delta v = 2$

Here, as in the $\Delta v = 1$ case, the computed rate constants are substantially smaller than the empirical values. (The CC rate constants are negligibly small, since we have so far completed CC cross section calculations that include $\Delta v = 2$ only through the first three energies.) In this case, however, the CS and classical calculations predict different peak locations for the rate constants – the classical rate constants showing a clear peak at $j_f = 24$, and the CS figures appearing to peak closer to $j_f = j_i = 4$.

5.2 Conclusions and Future Work

One feature that stands out prominently in these comparisons is the roughly equal failure of both the CS quantum and the classical rate constant calculations to accurately model the experimentally measured rate constants for $\Delta v = 1$ and 2. The disagreement is particularly interesting in the classical case, since recent classical trajectory calculations for $(v_i = 2, j_i = 30)$ on the same Li_2 $A^1\Sigma_u^+ - Ne$ potential energy surface have shown good agreement with experiment for the case of vibration-changing collisions, in both the magnitudes of the rate constants and the shapes of their distributions [GS95].

Near-perfect agreement among the CS quantum, classical, and empirical results for vibrationally inelastic collisions cannot of course be expected, since the CS and classical models are both fundamentally approximations of the truth. At least one previous study has suggested that classical rate constant calculations for Li_2 $A^1\Sigma_u^+ - Ne$ will show increasingly poorer agreement of rotationally summed vibrationally inelastic rate constants with experiment for $v_i \leq 3$ as v_i decreases, as illustrated in Fig. 5.8 [GGDMS96].

In continuing this program of research, we will seek to extend the quan-

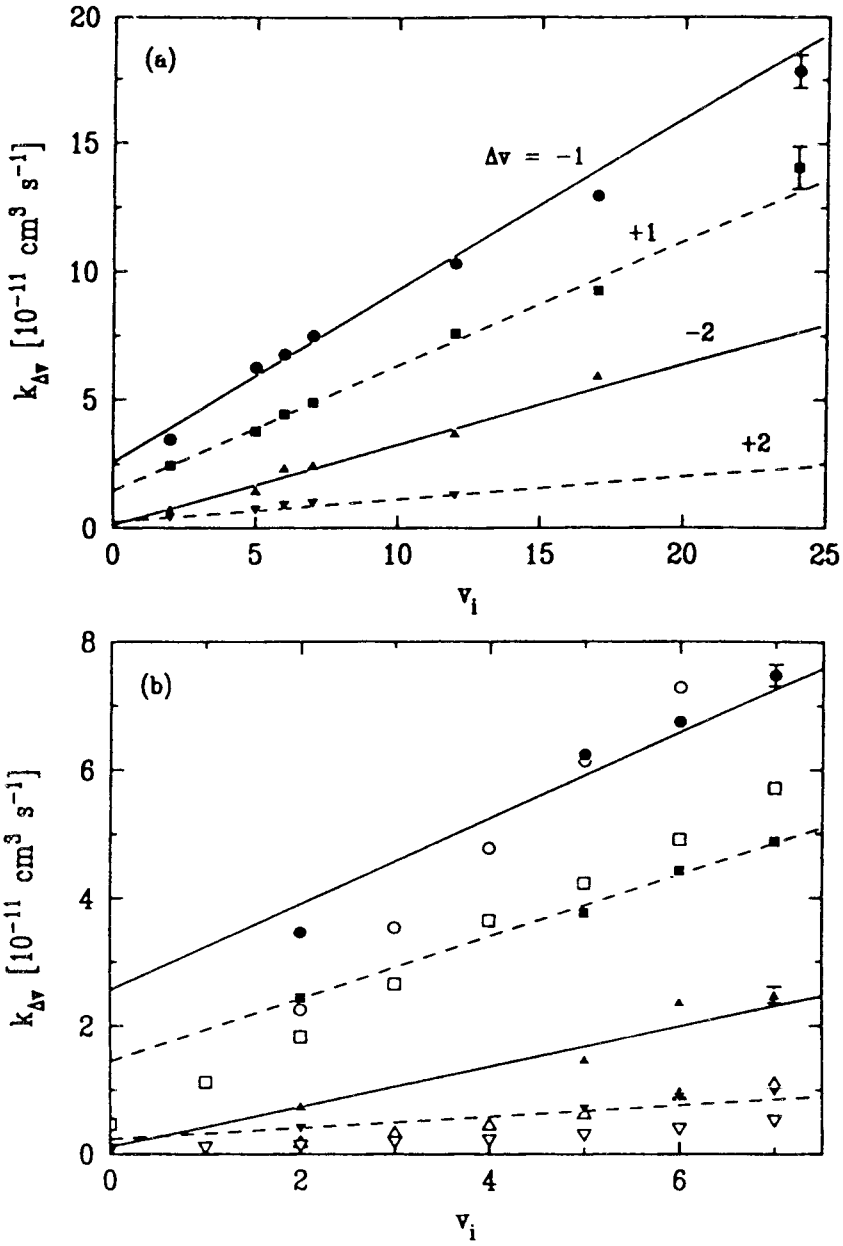

Figure 5.8: Fig. 11, excerpted from [GGDMS96]. Total (rotationally summed) vibrationally inelastic rate constants are plotted as a function of v_i. The upper graph shows experimentally obtained rate constants (symbols) and their least-squares linear fits (lines). The lower graph is an enlargement of the first, with rate constants computed classically on the Alexander-Werner Li_2 $A^1\Sigma_u^+ - Ne$ PES added (open symbols). Note in particular the disagreement between the fit line for $\Delta v = 1$ (upper dashed line) and the classical calculations (open squares) in either direction from the crossing at $v_i = 3.5$.

tum scattering calculations to provide for a more complete comparison with experiment. While the extreme computationally intensive nature of the exact CC calculations places an effective ceiling on the collision energies (and hence vibrational levels) that are reachable via this method, a few more CC calculations are still possible. A CC calculation currently underway should yield accurate quantum mechanical cross sections for vibrationally elastic collisions ($\Delta v = 0$) at the sixth Gauss-Laguerre energy (2644 cm^{-1}), and a properly optimized CC calculation that includes $\Delta v = 0$ and 1 should be possible at the fourth sample energy (1791 cm^{-1}). As we approach fundamental practical computational limits, we will have to seek ways to safely extrapolate rate constants based on the computable cross section information. I look forward to seeing the results of this research, and hope that the relevant sections of this thesis will serve as a useful preliminary guide to students who may continue this project in the near future.

Appendix A

Quantum Mechanically Computed Rate Constants

All rate constants are listed in units of cm^3 $molecule^{-1}$ s^{-1}.

j_f	**CS Rate Constant**	**CC Rate Constant**
0	2.421936e-11	1.831503e-11
2	1.635444e-10	1.138391e-10
6	2.733181e-10	1.999005e-10
8	1.746547e-10	1.435195e-10
10	1.318485e-10	1.216212e-10
12	9.930909e-11	1.030905e-10
14	7.773714e-11	8.222076e-11
16	6.290920e-11	6.511614e-11
18	4.872878e-11	5.353277e-11
20	3.591231e-11	4.439726e-11
22	2.774623e-11	3.734110e-11
24	2.194933e-11	2.967964e-11
26	1.715311e-11	2.301567e-11
28	1.297868e-11	1.814020e-11
30	9.060624e-12	1.429417e-11
32	6.599467e-12	1.169046e-11
34	5.042792e-12	9.329073e-12
36	3.813851e-12	6.812500e-12
38	2.824304e-12	4.713909e-12
40	1.916516e-12	3.320883e-12
42	1.262760e-12	2.250968e-12
44	8.793000e-13	1.834564e-12
46	6.022882e-13	1.404452e-12
48	4.044142e-13	8.700879e-13
50	2.535222e-13	4.461832e-13
52	1.537898e-13	1.542304e-13
54	1.075753e-13	1.710506e-14
56	7.804030e-14	4.397064e-16
58	5.682348e-14	4.313888e-18
60	3.818355e-14	3.555402e-20
62	2.232991e-14	-
64	1.556985e-14	-
66	1.077621e-14	-
68	7.584723e-15	-
70	4.647043e-15	-
72	3.572781e-15	-
74	1.987575e-15	-
76	1.289056e-15	-
78	1.011842e-15	-
80	7.710954e-16	-
82	5.727599e-16	-
84	3.566684e-16	-
86	2.746107e-16	-
88	1.595964e-16	-
90	5.605447e-17	-

Table A.1: $v_i = 0$, $j_i = 4$, $\Delta v = 0$

j_f	**CS Rate Constant**	**CC Rate Constant**
0	1.028722e-14	1.519937e-15
2	5.672654e-14	7.912483e-15
4	1.461568e-13	1.549184e-14
6	1.105936e-13	1.780873e-14
8	1.096548e-13	1.987259e-14
10	1.041537e-13	2.175169e-14
12	9.613297e-14	2.260431e-14
14	9.429719e-14	2.224605e-14
16	9.124339e-14	2.075446e-14
18	8.277341e-14	1.861848e-14
20	7.152158e-14	1.610048e-14
22	6.188675e-14	1.455669e-14
24	5.568119e-14	1.297138e-14
26	5.213955e-14	8.977644e-15
28	4.777865e-14	4.443740e-15
30	4.134835e-14	1.812453e-15
32	3.278069e-14	8.714693e-16
34	2.568173e-14	4.637247e-16
36	2.057616e-14	8.247301e-17
38	1.804091e-14	7.684155e-18
40	1.618213e-14	6.803880e-19
42	1.491340e-14	-
44	1.246190e-14	-
46	1.169420e-14	-
48	9.610814e-15	-
50	1.028876e-14	-
52	1.286924e-14	-
54	1.447787e-14	-
56	1.620937e-14	-
58	1.187389e-14	-
60	6.055316e-15	-
62	4.336868e-15	-
64	4.043095e-15	-
66	3.577316e-15	-
68	3.159779e-15	-
70	2.696798e-15	-
72	1.608526e-15	-
74	8.170970e-16	-
76	6.209925e-16	-
78	6.125945e-16	-
80	5.967794e-16	-
82	5.033449e-16	-
84	4.217816e-16	-
86	2.602082e-16	-
88	1.073873e-16	-
90	2.758459e-17	-

Table A.2: $v_i = 0$, $j_i = 4$, $\Delta v = 1$

j_f	**CS Rate Constant**	**CC Rate Constant**
0	1.105917e-15	2.800912e-18
2	6.004648e-15	1.719520e-17
4	1.436542e-14	3.024043e-17
6	1.210122e-14	3.000916e-17
8	1.219948e-14	1.948647e-17
10	1.225815e-14	7.961613e-18
12	1.211809e-14	1.708813e-18
14	1.183572e-14	-
16	1.116425e-14	-
18	1.005812e-14	-
20	9.243402e-15	-
22	8.827957e-15	-
24	7.923141e-15	-
26	6.088356e-15	-
28	4.199547e-15	-
30	3.273076e-15	-
32	3.112034e-15	-
34	3.361190e-15	-
36	3.708160e-15	-
38	3.604321e-15	-
40	2.832058e-15	-
42	1.770293e-15	-
44	1.023134e-15	-
46	7.994803e-16	-
48	9.381703e-16	-
50	1.278560e-15	-
52	1.764803e-15	-
54	1.957795e-15	-
56	1.171810e-15	-
58	8.411316e-16	-
60	8.398624e-16	-
62	8.615247e-16	-
64	8.257892e-16	-
66	7.790474e-16	-
68	5.476017e-16	-
70	2.568505e-16	-
72	1.434345e-16	-
74	1.259780e-16	-
76	1.213529e-16	-
78	1.039739e-16	-
80	8.255623e-17	-
82	6.033874e-17	-
84	3.574198e-17	-
86	1.421635e-17	-
88	2.675608e-18	-
90	2.102701e-19	-

Table A.3: $v_i = 0$, $j_i = 4$, $\Delta v = 2$

Appendix B

Experimentally Obtained Rate Constants

All rate constants are listed in units of cm^3 $molecule^{-1}$ s^{-1}. Error estimates are given both in cm^3 $molecule^{-1}$ s^{-1} and as a fraction of the corresponding rate constant.

j_f	**Rate Constant**	**Error**	**Fractional Error**
0	2.452000e-11	1.420000e-12	0.057912
6	2.295000e-10	3.260000e-11	0.142048
8	2.104000e-10	2.640000e-11	0.125475
10	1.687000e-10	1.400000e-11	0.082988
12	1.215000e-10	1.590000e-11	0.130864
14	1.330000e-10	2.330000e-11	0.175188
16	8.582000e-11	1.170000e-12	0.013633
18	7.308000e-11	1.740000e-12	0.023810
20	6.200000e-11	2.100000e-12	0.033871
22	5.558000e-11	5.070000e-14	0.000912
24	4.552000e-11	9.850000e-13	0.021639
26	3.807000e-11	1.290000e-12	0.033885
28	2.378000e-11	6.050000e-14	0.002544
30	2.134000e-11	8.530000e-13	0.039972
32	1.955000e-11	2.110000e-12	0.107928
34	1.361000e-11	5.870000e-13	0.043130
36	1.564000e-11	6.180000e-13	0.039514
38	9.633000e-12	2.330000e-13	0.024188
40	6.777000e-12	4.430000e-13	0.065368
42	6.184000e-12	1.980000e-13	0.032018
44	4.172000e-12	3.740000e-13	0.089645
46	5.039000e-12	2.220000e-13	0.044056
48	2.463000e-12	5.670000e-13	0.230207
50	1.810000e-12	4.030000e-13	0.222652
52	1.454000e-12	1.680000e-13	0.115543
54	1.136000e-12	3.100000e-14	0.027289
56	7.053000e-13	1.910000e-13	0.270807
58	5.905000e-13	1.200000e-13	0.203218
60	6.657000e-13	1.400000e-13	0.210305
62	2.933000e-13	1.390000e-13	0.473917
64	5.954000e-13	7.310000e-14	0.122775
66	2.531000e-13	3.810000e-14	0.150533
68	2.074000e-13	2.220000e-14	0.107040
72	1.122000e-13	1.860000e-14	0.165775
76	5.517000e-14	3.230000e-15	0.058546
78	5.126000e-14	1.780000e-14	0.347249
80	1.476000e-13	1.240000e-13	0.840108
82	3.492000e-14	2.870000e-14	0.821879
86	3.014000e-14	5.250000e-15	0.174187

Table B.1: $v_i = 0$, $j_i = 4$, $\Delta v = 0$

j_f	**Rate Constant**	**Error**	**Fractional Error**
2	1.087000e-13	8.800000e-15	0.080957
4	1.544000e-13	2.250000e-14	0.145725
6	2.108000e-13	1.330000e-14	0.063093
8	2.626000e-13	1.940000e-14	0.073877
10	1.724000e-13	1.830000e-15	0.010615
12	3.921000e-13	2.310000e-14	0.058914
14	1.772000e-13	3.110000e-14	0.175508
16	2.606000e-13	1.640000e-14	0.062932
18	4.339000e-13	2.120000e-14	0.048859
20	1.828000e-13	2.030000e-14	0.111050
22	7.359000e-13	1.100000e-14	0.014948
24	5.030000e-13	3.720000e-14	0.073956
26	4.365000e-13	7.240000e-15	0.016586
28	1.758000e-13	9.510000e-14	0.540956
30	4.102000e-13	1.540000e-14	0.037543
32	5.272000e-13	1.510000e-13	0.286419
34	1.621000e-13	7.570000e-15	0.046700
36	2.822000e-13	4.590000e-14	0.162651
38	3.712000e-13	5.140000e-14	0.138470
40	2.975000e-13	5.960000e-14	0.200336
42	1.552000e-13	2.960000e-14	0.190722
44	1.664000e-13	9.130000e-15	0.054868
46	1.694000e-13	3.240000e-14	0.191263
48	2.382000e-13	1.430000e-14	0.060034
50	2.394000e-13	1.300000e-14	0.054302
52	1.753000e-13	7.860000e-14	0.448374
54	1.902000e-13	3.370000e-14	0.177182
56	1.284000e-13	1.180000e-14	0.091900
60	3.671000e-14	6.890000e-16	0.018769
62	1.324000e-13	2.600000e-14	0.196375
64	1.342000e-13	2.640000e-14	0.196721
66	4.335000e-14	2.410000e-14	0.555940
68	1.055000e-13	1.550000e-14	0.146919
76	1.299000e-13	9.910000e-14	0.762895
78	2.446000e-14	1.460000e-14	0.596893

Table B.2: $v_i = 0$, $j_i = 4$, $\Delta v = 1$

j_f	**Rate Constant**	**Error**	**Fractional Error**
2	3.761000e-14	1.540000e-14	0.409466
6	1.379000e-13	2.440000e-14	0.176940
8	1.351000e-13	1.130000e-13	0.836417
10	1.601000e-13	3.260000e-14	0.203623
12	1.321000e-13	5.630000e-15	0.042619
14	4.668000e-14	2.200000e-14	0.471294
16	1.542000e-13	2.790000e-14	0.180934
18	9.885000e-14	2.970000e-14	0.300455
26	4.731000e-13	4.140000e-14	0.087508
28	1.965000e-13	8.730000e-16	0.004443
30	1.575000e-13	1.140000e-13	0.723810
32	1.225000e-13	3.200000e-14	0.261224
34	5.848000e-14	2.920000e-14	0.499316
36	3.891000e-13	4.780000e-14	0.122848
42	1.755000e-13	2.570000e-14	0.146439
48	6.248000e-14	9.020000e-15	0.144366
50	6.500000e-14	1.390000e-14	0.213846
56	3.118000e-14	4.180000e-15	0.134060
58	5.315000e-14	1.260000e-14	0.237065
60	5.310000e-14	7.860000e-15	0.148023
64	6.440000e-14	5.100000e-14	0.791925
68	4.124000e-14	4.740000e-15	0.114937
74	2.730000e-14	1.030000e-14	0.377289
76	1.077000e-14	3.540000e-15	0.328691
88	7.977000e-14	2.530000e-14	0.317162

Table B.3: $v_i = 0$, $j_i = 4$, $\Delta v = 2$

Appendix C

Classically Computed Rate Constants

All rate constants are listed in units of cm^3 $molecule^{-1}$ s^{-1}. Error estimates are given both in cm^3 $molecule^{-1}$ s^{-1} and as a fraction of the corresponding rate constant.

j_f	**Rate Constant**	**Error**	**Fractional Error**
0	5.275575e-11	9.633739e-13	0.018261
2	3.073295e-10	2.486443e-12	0.008090
6	5.112689e-10	3.129373e-12	0.006121
8	3.331178e-10	2.378616e-12	0.007140
10	2.645383e-10	2.079408e-12	0.007861
12	2.259830e-10	1.915659e-12	0.008477
14	1.712124e-10	1.701966e-12	0.009941
16	1.342898e-10	1.548118e-12	0.011528
18	1.044940e-10	1.372689e-12	0.013137
20	8.606812e-11	1.274648e-12	0.014810
22	7.324549e-11	1.182444e-12	0.016144
24	5.686868e-11	1.015850e-12	0.017863
26	4.375167e-11	8.559885e-13	0.019565
28	3.254813e-11	6.999071e-13	0.021504
30	2.581512e-11	6.234949e-13	0.024152
32	2.074082e-11	5.560879e-13	0.026811
34	1.573149e-11	4.759702e-13	0.030256
36	1.123235e-11	3.752758e-13	0.033410
38	7.148718e-12	2.581200e-13	0.036107
40	4.707986e-12	1.721648e-13	0.036569
42	3.095568e-12	9.285715e-14	0.029997
44	2.422007e-12	6.670180e-14	0.027540
46	1.900237e-12	5.750261e-14	0.030261
48	1.371899e-12	4.753007e-14	0.034645
50	8.348514e-13	3.224731e-14	0.038626
52	5.222630e-13	2.176278e-14	0.041670
54	3.755987e-13	1.502747e-14	0.040009
56	3.066641e-13	1.307034e-14	0.042621
58	2.395943e-13	1.153839e-14	0.048158
60	1.487841e-13	8.870314e-15	0.059619
62	1.064648e-13	7.040060e-15	0.066126
64	5.274228e-14	4.201588e-15	0.079663
66	3.015674e-14	2.177660e-15	0.072211
68	2.625286e-14	1.667744e-15	0.063526
70	2.096970e-14	1.492246e-15	0.071162
72	1.411897e-14	1.227919e-15	0.086969
74	8.715418e-15	9.344542e-16	0.107219
76	4.571959e-15	6.318857e-16	0.138209
78	1.377548e-15	1.788365e-16	0.129822
80	8.459596e-16	1.041305e-16	0.123092
82	6.595230e-16	9.327062e-17	0.141421
84	4.458907e-16	7.646960e-17	0.171499
86	3.535248e-16	7.070495e-17	0.200000
88	2.809990e-16	6.283308e-17	0.223606
90	7.383630e-17	3.302058e-17	0.447213

Table C.1: $v_i = 0$, $j_i = 4$, $\Delta v = 0$

j_f	**Rate Constant**	**Error**	**Fractional Error**
0	1.783322e-14	1.921950e-15	0.107774
2	6.395908e-14	3.431267e-15	0.053648
4	1.177771e-13	4.508997e-15	0.038284
6	1.396442e-13	4.939466e-15	0.035372
8	1.385626e-13	4.927203e-15	0.035559
10	1.254774e-13	4.756651e-15	0.037908
12	1.218796e-13	5.078452e-15	0.041668
14	1.153650e-13	4.922785e-15	0.042671
16	1.007327e-13	4.989765e-15	0.049535
18	7.981085e-14	4.520005e-15	0.056634
20	6.672561e-14	3.993467e-15	0.059849
22	5.609507e-14	3.427609e-15	0.061104
24	4.534913e-14	3.068291e-15	0.067659
26	4.052363e-14	2.765758e-15	0.068250
28	5.351505e-14	3.516650e-15	0.065713
30	4.142102e-14	2.961449e-15	0.071496
32	4.604218e-14	3.541468e-15	0.076918
34	4.918089e-14	3.626087e-15	0.073730
36	4.907661e-14	3.758657e-15	0.076588
38	3.974556e-14	3.047240e-15	0.076669
40	4.543474e-14	3.504406e-15	0.077131
42	4.182092e-14	3.464570e-15	0.082843
44	4.193336e-14	3.585330e-15	0.085501
46	3.779887e-14	3.467554e-15	0.091737
48	2.853353e-14	2.786500e-15	0.097657
50	2.188757e-14	2.087047e-15	0.095353
52	2.464468e-14	2.161138e-15	0.087692
54	3.253072e-14	3.017957e-15	0.092773
56	3.133678e-14	2.994197e-15	0.095549
58	2.670599e-14	2.702189e-15	0.101183
60	2.002485e-14	2.224168e-15	0.111070
62	1.819841e-14	1.875628e-15	0.103065
64	1.413619e-14	1.151318e-15	0.081445
66	1.275571e-14	1.118348e-15	0.087674
68	1.123238e-14	1.061251e-15	0.094481
70	7.621290e-15	8.546326e-16	0.112138
72	5.540490e-15	7.122948e-16	0.128562
74	1.427174e-15	2.428168e-16	0.170138
76	7.467239e-16	9.407824e-17	0.125988
78	5.580771e-16	8.319309e-17	0.149071
80	5.006079e-16	7.724558e-17	0.154304
82	6.043063e-16	8.632958e-17	0.142857
84	4.627351e-16	7.712251e-17	0.166667
86	3.678773e-16	7.079791e-17	0.192450
88	1.501413e-16	4.526938e-17	0.301512

Table C.2: $v_i = 0$, $j_i = 4$, $\Delta v = 1$

j_f	**Rate Constant**	**Error**	**Fractional Error**
0	5.371947e-17	2.200748e-17	0.409674
2	7.650380e-16	2.743337e-16	0.358588
4	7.197882e-16	2.443275e-16	0.339444
6	4.741222e-15	8.306951e-16	0.175207
8	5.566416e-15	7.502702e-16	0.134785
10	7.137600e-15	7.695349e-16	0.107814
12	1.186196e-14	1.041437e-15	0.087796
14	1.459460e-14	1.284208e-15	0.087992
16	1.793035e-14	1.545040e-15	0.086169
18	2.072780e-14	1.823652e-15	0.087981
20	1.825901e-14	1.659530e-15	0.090888
22	2.175182e-14	1.933839e-15	0.088905
24	2.752067e-14	2.310514e-15	0.083956
26	2.065549e-14	2.037739e-15	0.098654
28	1.963207e-14	2.019940e-15	0.102890
30	1.493206e-14	1.736795e-15	0.116313
32	1.446007e-14	1.733133e-15	0.119856
34	7.021927e-15	1.064200e-15	0.151554
36	5.991317e-15	7.856007e-16	0.131123
38	4.991740e-15	4.830662e-16	0.096773
40	6.852785e-15	7.504673e-16	0.109513
42	6.246435e-15	6.999895e-16	0.112062
44	6.030478e-15	6.784955e-16	0.112511
46	6.177776e-15	7.504929e-16	0.121483
48	6.580226e-15	8.039538e-16	0.122177
50	6.175342e-15	9.682160e-16	0.156787
52	4.813842e-15	7.480397e-16	0.155393
54	7.586124e-15	1.313799e-15	0.173184
56	3.528119e-15	6.598857e-16	0.187036
58	2.521056e-15	3.152737e-16	0.125056
60	2.953756e-15	3.984065e-16	0.134881
62	3.157466e-15	4.364259e-16	0.138220
64	3.080517e-15	4.597118e-16	0.149232
66	3.435544e-15	4.974657e-16	0.144800
68	4.029744e-15	5.688879e-16	0.141172
70	2.155574e-15	3.815188e-16	0.176992
72	1.018104e-15	1.061446e-16	0.104257
74	9.199309e-16	1.028515e-16	0.111804
76	8.059809e-16	9.773958e-17	0.121268
78	5.392679e-16	8.129778e-17	0.150756
80	5.071779e-16	7.920794e-17	0.156174
82	3.766575e-16	6.764960e-17	0.179605
84	2.264605e-16	5.337743e-17	0.235703
86	1.000382e-16	3.536883e-17	0.353553

Table C.3: $v_i = 0$, $j_i = 4$, $\Delta v = 2$

Bibliography

[Al84] Millard H. Alexander, *J. Chem. Phys.* **81**, 4510 (1984).

[AM87] Millard. H. Alexander and D. E. Manolopoulos, *J. Chem. Phys.* **86**, 2044 (1987).

[AW91] Millard H. Alexander and Hans-Joachim Werner, *J. Chem. Phys.* **95**, 6524-6535 (1991).

[ArWe95] George Brown Arfken and Hans-Jurgen Weber, *Mathematical Methods for Physicists*, Academic Press, San Diego, California, 1995.

[Ba83] Ralph Baierlein, *Newtonian Dynamics*, McGraw-Hill, New York, New York, 1983.

[BS95] Andrew Billeb and Brian Stewart, *Chem. Phys. Lett.* **247**, 433-439 (1995).

[Da92] Scott R. Davis, "Experimentally Measuring the Velocity Dependence of Vibrotational Transfer in Atom-Diatom Collisions", B.A. Thesis, Physics Department, Wesleyan University (1992).

[Ga96] Yunxiao Gao, "Initial State Dependence of Collisional Energy Transfer in $Li_2^* - Ne$", Ph.D. Thesis, Physics Department, Wesleyan University (1996).

[GGDMS96] Yunxiao Gao, Peter S. Gorgone, Scott Davis, Eric K. McCall, and Brian Stewart, *J. Chem. Phys.* **104**, 1415 (1996).

[GS95] Yunxiao Gao and Brian Stewart, *J. Chem. Phys. Communications* **103**, 860-863 (1995).

[St87] Brian Auber Stewart, "Vibration-Rotation Resonance in Inelastic $Li_2^* - Ne$ Collisions", Ph.D. Thesis, Chemistry Department, Massachusetts Institute of Technology (1987).

[Gd69] R. G. Gordon, *J. Chem. Phys.* **51**, 14 (1969).

[Gd71] R. G. Gordon, *Meth. Comput. Phys.* **10**, 81 (1971).

[Go91] Peter Samuel Gorgone, "A Study of Vibrotational Transfer in Atom-Diatom Collisions", B.A. Thesis, Physics Department, Wesleyan University (1991).

[Hib] D. E. Manolopoulos, *J. Chem. Phys.* **85**, 6425 (1986); Millard H. Alexander and D. E. Manolopoulos, *J. Chem. Phys.* **86**, 2044 (1987). HIBRIDON^{TM} is a package of programs for the time-independent quantum treatment of inelastic collisions and photodissociation written by M. H. Alexander, D. E. Manolopoulos, H.-J. Werner, and B. Follmeg, with contributions by P. F. Vohralik, D. Lemoine, G. Corey, R. Gordon,

B. Johnson, T. Orlikowski, A. Berning, A. Degli-Esposti, C. Rist, P. Dagdigian, B. Pouilly, G. van der Sanden, M. Yang, and F. de Weerd.

[HibDoc] Millard H. Alexander, *Hibridon* documentation. (WWW: `http://mha-mac1.umd.edu/~mha/hibridon/`).

[Jo73] B. R. Johnson, *J. Comput. Phys.* **13**, 445 (1973).

[Jo79] B. R. Johnson, *Proceedings of the NRCC Workshop on Algorithms and Computer Codes in Atomic and Molecular Scattering Theory*, edited by L. D. Thomas (Lawrence Berkeley Laboratory, CA Report LBL-9501 l979) pp. 86-92 (Vol. I) and p. 52 (Vol. II).

[Ma86] D. E. Manolopoulos, *J. Chem. Phys.* **85**, 6425 (1986).

[MB89] John Normal Murrell and Slobodan D. Bosanac, *Introduction to the Theory of Atomic and Molecular Collisions*, John Wiley and Sons, West Sussex, England, 1989.

[MS83] F. Mrugala and D. Secrest, *J. Chem. Phys.* **78**, 5954 (1983).

[Pa79] M. D. Pattengill, in *Atom-Molecule Collision Theory: A Guide for the Experimentalist*, Plenum, New York, New York, 1979.

[Sm86] N. Smith, *J. Chem. Phys.* **85**, (1986).

[WM77] P.H. Wine and L.A. Melton, *Chem. Phys. Lett.* **45**, 509 (1977).

Typeset using LaTeX.